PHYSICAL REVIEW FLUIDS **2**, 064202 (2017)

# Flow fields and vortex dynamics of bubbles collapsing near a solid boundary

Fabian Reuter,[1,*] Silvestre Roberto Gonzalez-Avila,[2] Robert Mettin,[1] and Claus-Dieter Ohl[2]
[1]*Christian Doppler Laboratory for Cavitation and Micro-Erosion, Drittes Physikalisches Institut,*
*Georg-August-Universität Göttingen, Friedrich-Hund-Platz 1, 37077 Göttingen, Germany*
[2]*School of Physical and Mathematical Sciences, Nanyang Technological University,*
*21 Nanyang Link, 637371 Singapore*

(Received 6 December 2016; published 13 June 2017)

When a cavitation bubble oscillates and collapses in the vicinity of a solid boundary (a substrate), it induces intense microconvection in the surrounding liquid and—of high practical importance—directly at the substrate. As the involved flows are fast, highly unsteady, and possess an impressive shear, experiments are difficult and data are scarce. Here, insight into the generation and dynamics of the liquid flows from individual cavitation bubbles collapsing in the vicinity of a solid boundary is provided. Single laser-induced cavitation bubbles (maximum radius around 375 $\mu$m) are seeded at precisely defined standoff distances to a substrate by a focused laser pulse. The bubble shape dynamics are imaged by synchronized high-speed cameras from two perpendicular viewing angles. Recording of the shape dynamics is combined with the simultaneous time-resolved measurement of the full flow field on a micrometer-resolution. Measurements employ a high-speed hybrid particle imaging velocimetry and particle tracking velocimetry technique, with a temporal sampling of up to 135 kHz, using fluorescent microparticles as tracers. The time evolution of the unsteady flow field induced by one and the same bubble over a time period much longer than the bubble lifetime is determined. The shear flow at the substrate is analyzed and a liquid transport toward and away from the substrate surface is demonstrated. Depending on the bubble standoff distance, very different flow patterns are observed. The dominant liquid displacement is caused by the long-lived vortex ring being produced during bubble collapse. Most peculiar, the bubble standoff distance determines the sense of direction of the circulation associated with the vortex ring and, consequently, whether the vortex is ejected from the substrate or radially stretches over it. The results are relevant for the understanding of cavitation effects, such as surface cleaning, erosion, and mixing or in biomedical context and may serve as basis for numerical simulations.

DOI: 10.1103/PhysRevFluids.2.064202

## I. INTRODUCTION

Cavitation is an important phenomenon occurring in hydrodynamic flows and intense ultrasonic fields, involving nucleation, oscillation, and collapse of bubbles. Indeed, many applications of ultrasound rely to a large extent on the utilization of effects induced by collapsing bubbles [1–3]. Typically, cavitation bubbles develop in a statistical manner forming clouds of hundreds or thousands of bubbles of different sizes, and the individual bubble behavior is a result of complex multibubble interaction. Consequently, cavitation effects emerge and interfere in a complicated and often unforeseeable way. But a deeper understanding of the cavitation phenomena is crucial for a controlled and targeted utilization of cavitation. To reduce complexity and assure repeatability of experiments, the detailed collapse dynamics of bubbles is investigated here in single-bubble studies.

A single cavitation bubble is a strongly nonlinear oscillator [4]. Its energy is converted continually between different forms as the bubble oscillates. The gas in the bubble is compressed, heat is generated, chemical reactions set in, and light and acoustic emissions occur. Furthermore, of particularly practical importance, kinetic energy is transferred to the surrounding liquid producing

---

[*] freuter@uni-goettingen.de

intense microconvection. When there is some geometric asymmetry in the bubble or its surroundings, for example, by deviations from a spherical bubble shape, a pressure gradient, or by the presence of a boundary, the bubble dynamics are dramatically affected. Then, during the cascades of energy conversion the bubble changes shape, it generally translates, and depending on where the conversion to kinetic energy takes place, very different flow field patterns can be generated. This leads to an outstanding characteristic of oscillating and collapsing cavitation bubbles: their ability to generate intense shear flows, in particular when a bubble collapse takes place close to a solid wall. This potential of transient bubbles, to be avoided where erosion from hydrodynamic cavitation is an issue, is beneficially exploited in ultrasonic cleaning and ultrasonic mixing, which more precisely would be called "cleaning or mixing by ultrasonically driven bubbles" [5]. Further important applications are found in a biomedical context, for example, in sonoporation and drug delivery or laser surgery; see, for example, Refs. [6–8]. However, the knowledge of the unsteady flow fields generated by aspherically collapsing bubbles is still incomplete.

Referring to experiments on single bubbles, transient bubbles were generated at confined positions by spark generation [9–11], which, however, has the disadvantage of being invasive as the electrode in the liquid are in contact with the cavity. Lauterborn noninvasively seeded single bubbles by focusing a laser pulse into a liquid [12]. Thereafter, many more details of the shape dynamics of a bubble collapsing in the vicinity of a solid boundary were discovered, both experimentally [13,14] and numerically [15–17]. It is well known that the oscillation and collapse of a cavitation bubble in the vicinity of a solid boundary leads to the formation of a jet flow, which is usually directed toward the solid and pierces the bubble [13,18,19]. In this way, it leaves the bubble in a toroidal shape, initiating characteristic torus bubble dynamics [20–22]. As the jet impacts onto the solid wall, it is redirected and further effects such as splashing occur [23,24]. A shock wave is emitted [25,26] and a vortex ring, also called toroidal vortex, that tends to trap remnant gas entities, can be formed [10,13,14,27–29]. All these phenomena can be well perceived experimentally by the imaging of the bubble shape dynamics or by simulations [30], whereas the knowledge about the simultaneously actuated microconvection generated during bubbles collapse is scarcer because of experimental difficulties.

In contrast, the microstreaming associated with bubbles *stably* oscillating in the vicinity of a solid boundary is much slower, and the stable bubbles show merely volume pulsations. Some experimental data is available for instance from a microparticle imaging velocimetry technique [31–33] and theoretical derivations [34]. For more vigorously collapsing bubbles experimental demands increase from the high dynamic range exhibited by the transient streaming that occurs on microscales, the high shear rates, and the rapidly deforming interfaces between the three phases in the flow (gas, liquid, and solid). Also, numerical demands increase, to a large extent from topology changes, as collapsing bubble develop several instabilities such as Rayleigh-Tayler instabilities or parametric instabilities [30,35,36].

The effect of microconvection generated by single bubbles collapsing on a solid substrate was measured by erosion tests [37], by anemometry [38], by hydrodynamic modelling according to the high-speed imaging of the shape dynamics [39–41], by particle removal [29] and by a chronoamperometric technique [42]. Furthermore the generated microconvection was considered by numerical simulations [24,43]. Vogel and Lauterborn [44], Vogel *et al.* [28] pioneered in the measurement of the entire flow field around a single collapsing bubble by using a particle tracking method and a drum camera operated at 10 000 fps (frames per second). They imaged scattered light from 25-$\mu$m-diameter Vestamid particles to obtain local velocities at scattered positions. Kröninger *et al.* [45] used digital particle tracking technique with 5-$\mu$m-diameter fluorescent polystyrene particles. Their camera could only record two images per bubble and they combined data from repeated experiments to increase spatial and temporal resolution. Therefore, a long-term measurement of the flow fields was not possible as small deviations in the initial conditions accumulate and result in different flow fields.

In this work, we apply an adapted time-resolved fluorescent particle tracking velocimetry and particle image velocimetry ($\mu$PIV/PTV) technique and measure the highly unsteady flow field during bubble collapse in the vicinity of a solid boundary as well as its long-term evolution. With long-term in the case of a collapsing microbubble we refer to only a few milliseconds, still about a hundred times longer than the time scale inherent to microbubble oscillations. This requires the measurement of the bubble-induced microconvection on one and the same bubble over the whole time-span. The flow field measurement is combined with simultaneous high-speed imaging of the shape of the bubble while it generates the flow field. Details on the experimental setup are given in Sec. II.

First the long-term gas shape dynamics alone are discussed in Sec. III: The bubble collapse in the vicinity of a solid substrate is analyzed by means of high-speed imaging and the shape of the micro-bubble is recorded synchronously from two viewing angles. It is found that after collapse with a vortex flow, remnant bubbles move either off the substrate, or along the substrate. In this context, we call the vortical flow either "*free vortex*" or "*wall vortex*" and find a sharp transition for their generation depending on the standoff distance.

In Sec. IV, for both vortex scenarios the time-resolved flow fields are presented together with the synchronously imaged bubble shapes. In particular, wall shear rates exhibited at the substrate and the vorticity associated with the vortices are analyzed.

In Sec. V, the potential of a collapsing bubble for micromixing and mass transfer enhancement, especially in the near-wall layer, is examined. For this purpose, the total liquid displacement, deduced from the time-resolved velocity fields, is illustrated by a technique we call *Lagrangian ink map*, a representation similar to the experimental flow visualization with the help of dyed liquid.

## II. EXPERIMENTAL

A $\mu$PIV/PTV setup for the time-resolved measurement of the flows generated by the collapse of a single, laser-seeded bubble near a rigid boundary is built. It employs two high-speed cameras and allows for the synchronized imaging of the bubble shape dynamics together with the measurement of the flow field. By the use of *video* cameras and a sufficient particle seeding density it permits the measurement of the flow evolution at one and the same bubble over its whole dynamics.

A simplified description of the setup for the particle imaging is given in Sec. II A. The setup for the recording of only the shape dynamics is described in Sec. II B. Further details and a discussion of the experimental setup and the data evaluation can be found in the Appendices.

### A. Flow field measurement

Single bubbles are created at confined positions by the optical breakdown induced by a pulsed nanosecond Nd:YAG-laser (Orion, New Wave, wavelength 532 nm, pulse duration approx. 6.5 ns, maximum pulse energy 15 mJ) in a water filled cuvette; see Fig. 1 for a sketch. The cuvette (cubic geometry, internal dimensions: $12 \times 12 \times 8\,\mathrm{mm}^3$) is made of an acrylic glass frame that is in-house modified to have optical glass windows at all six face plates for best optical properties for optical imaging and for coupling of the laser pulse through the top cover window. The cuvette is attached to a three-axis translational stage. Thereby, a positioning of the fixed laser focus within the cuvette is permitted, allowing for a precise control of the bubble standoff distance $\gamma$, which is given as the distance from the bubble center to the inner top cover boundary (see the inset in Fig. 1 for a geometric definition).

The cuvette is filled with distilled and degassed water and seeded with fluorescent velocimetry tracer particles for the measurement of the flow velocity field (Thermo Scientific, Fluoro-Max 36-2, polystyrene particles diameter $5\,\mu$m, volumetric mass density: $1.05\,\mathrm{g/cm}^3$, thus well-matched to the mass density of water within the lieu of the experiment duration of a few milliseconds). The fluorescence excitation is realized up to saturation level with the light of a second green laser (Nd:YAG CW, wavelength: 532 nm, power 400–1000 mW). An exemplary image of the light sheet in side projection, appearing bright by the fluorescing tracer particles, is given in Fig. 1.

The tracer particles in the flow field of the collapsing bubble are imaged by the *PIV camera*, a high-speed camera of type Photron Fastcam SA1.1 model 675K-M1, giving the *particle image*. It is coupled to a long-distance microscope (Infinity K2-CF4) and operated between 22 000 and 135 000 frames per second (fps). From the record rate, the minimum time step for the evaluation between

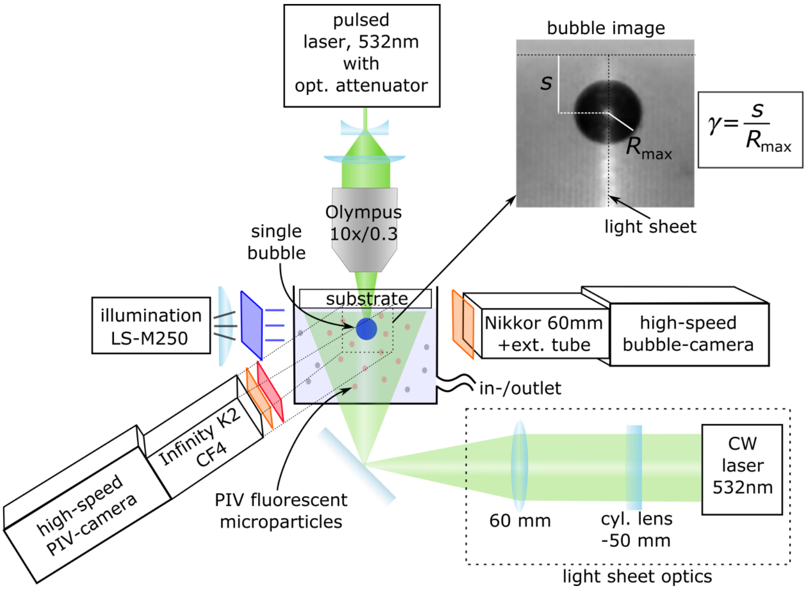

FIG. 1. Sketch of the high-speed $\mu$PIV/PTV setup and the devices for bubble seeding. See the inset in the upper right corner showing a sample image for a geometrical definition of $\gamma = \frac{s}{R_{max}}$. The laser sheet illumination appears bright and shows up as a vertical line in this side projection (see also the vertical dashed line). It has a thickness of about 140 $\mu$m and is adjusted to cut the plane where the laser-induced bubble is created. The solid boundary spans horizontally on top (see horizontal, dashed line).

two particle images is determined: $\Delta T_{\rm PIV} = 1/40\,000$ s to $1/135\,000$ s. The particle image exposure time was set between $T^{\rm e}_{\rm PIV} = 5.5\,\mu$s and 20 $\mu$s. The resolution of the camera is 4.5 $\mu$m/pixel, the depth of field is about 75 $\mu$m, and the field of view is about 2 mm × 1.3 mm (at 40 000 fps) or 1.2 mm × 0.5 mm (at 135 0000 fps).

With a second high-speed camera, the *bubble camera*, the bubble dynamics (the shape of the gas phase) is imaged simultaneously to the PIV-exposure (camera: Photron Fastcam SA1.1 model 675 K-C1, frame rate: 250 000 fps, interframe time $\Delta T_{\rm bub} = 4\,\mu$s; exposure time $T^{\rm e}_{\rm bub} = 370$ ns). The camera is oriented perpendicularly to the PIV camera and employs a Nikkor 60 mm objective with an extension tube (resolution: 13.5 $\mu$m/pixel).

The bubble camera is also used to determine the value of the standoff parameter $\gamma$ and the maximum bubble radius $R_{\max}$; for $\gamma \leqslant 1$, $R_{\max}$ is taken as the equivalent radius of a sphere with the same volume of the cavity. Furthermore, the bubble camera is used to confirm the accurate positioning of the light sheet and to verify the symmetry of the bubble to exclude inhomogeneously seeded bubbles from evaluation. Additionally, the bubble collapse time $T_{\rm c}$ (the time from maximum expansion to first collapse) and the bubble lifetime $T_{\rm L}$ (the time from bubble seeding by plasma generation to first collapse) are determined from the bubble-camera image. For a comparison of bubbles of differing sizes, times are given here also in a form normalized to the bubble lifetime: $\tau = t/T_{\rm L}$.

Further considerations of the experimental details are given the Appendices.

### B. High-speed imaging of the shape dynamics

In addition to the measurement of the flow fields, the shape dynamics of collapsing bubbles is recorded alone, synchronously from two perspectives. The shape dynamics imaging is carried out in the same cuvette as the PIV-measurements, described in Sec. II A. However, the setup is simplified and slightly modified, and for best imaging quality, no velocimetry tracers are present in the liquid

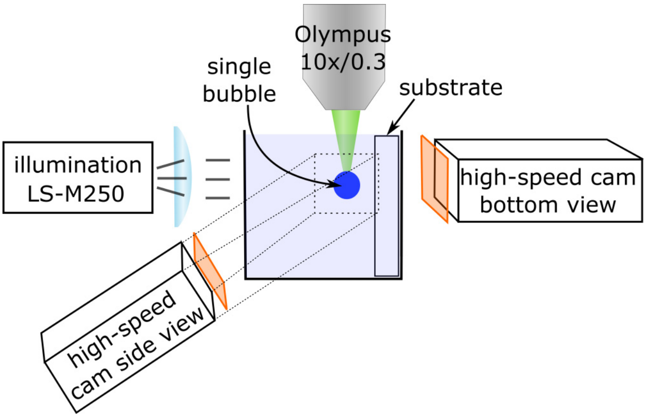

FIG. 2. Simplified setup for the imaging of the shape dynamics.

for now, as shown in Fig. 2 (see Sec. II A for the detailed description of the employed devices). In this configuration, for convenience, the substrate extends vertically (which leaves the bubble dynamics unaltered as buoyancy does not play a role here). Both cameras are operated synchronized at a frame rate of 180 000 fps (exposure time 370 ns), the spatial resolution is now 13.5 $\mu$m/pixel.

## III. BUBBLE SHAPE DYNAMICS AND INDUCED VORTEX FLOWS

The peculiar collapse dynamics of a bubble near a solid boundary has been subject of a number of studies that employed laser-induced bubbles and high-speed imaging to follow the bubble's shape. It was found that a collapsing bubble generates a jet flow. It is directed toward the solid boundary and pierces the bubble, leaving the bubble in a toroidal shape. The jet forms due to the asymmetry introduced by the solid boundary by inhibition of flow from the boundary side toward the originally radially collapsing bubble. Consequently, during collapse the bubble deforms and the liquid flow toward the boundary overweighs resulting in the formation of a jet (for further details on the jet, both experimental and theoretical; see, for example, Refs. [9,13–15,17,30,46]). Here though, we want to focus on the connection of collapse dynamics and subsequent development of vortex flows. Due to technical limitations of the recordings done by framing cameras, hitherto works mainly present either shorter time series or compositions from independently seeded bubbles. However, the detailed longer-term dynamics of a jetting bubble can be rather sensitive to the initial conditions, and longer continuous recordings are desirable. Therefore, we employ state of the art high-speed *video* cameras that allow for sequences covering the full duration of collapse and flow dynamics for one individual bubble. Furthermore, for shape visualization, two such cameras are operated from different perspectives (side view and bottom view) in a synchronized mode, which reveals otherwise partly hidden or unclear details (see Sec. II B and Fig. 2 for the experimental setup). We show in Sec. III A representative image series for the two observed cases of a bubble producing a ring vortex migrating toward the substrate (*wall vortex*) and a ring vortex migrating away from the substrate (*free vortex*). The respective vortices entrain remnant bubbles and can therefore be traced in the bubble shape imaging. A clear dependency on the standoff distance $\gamma$ is found, as reported afterward in Sec. III B.

### A. High-speed imaging series

For two bubbles collapsing in the vicinity of a solid substrate, long-time imaging series of bubble shapes are presented in Fig. 3; in the left columns, the bubble standoff distance is $\gamma = 1.21$, in the

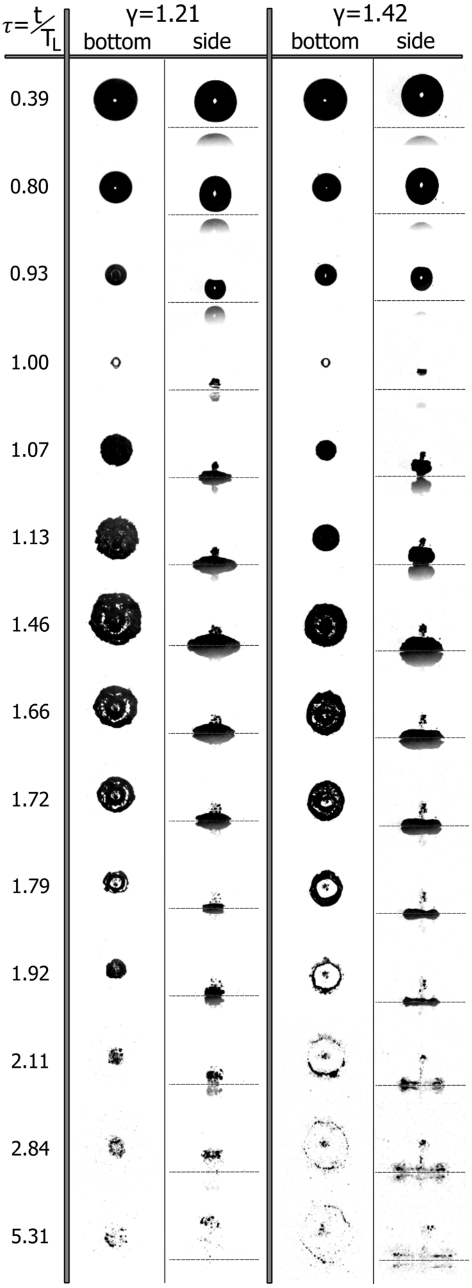

FIG. 3. Time series of two bubbles, one seeded at $\gamma = 1.21$, one at $\gamma = 1.42$ ($R_{\max} = 414\,\mu$m in both cases, $T_{\rm L}(\gamma = 1.21) = 85\,\mu$s, $T_{\rm L}(\gamma = 1.42) = 83\,\mu$s, camera exposure time: 360 ns). Each bubble is recorded from two perspectives simultaneously by two synchronized high-speed cameras: in bottom view and side view. In bottom view, the view direction is through the transparent solid substrate so that the jet is directed toward the observer. In side view, the solid boundary is located horizontally, below the bubble (dashed line). The boundary location also gets apparent by a mirror image of the gas phase on the substrate. Nondimensionalized times $\tau$ are given with respect to the bubble seeding (plasma generation). Despite the small standoff difference, the two bubbles exhibit very different dynamics after the first collapse. In Video 1 (Supplemental Material [48]) the respective movies from which the images were taken can be found.

right the bubble is generated at a slightly larger distance from the substrate: $\gamma = 1.42$. Each bubble is recorded from two viewing directions simultaneously: in bottom view, through the transparent substrate, in such a way that the bubble migrates toward the observer during collapse, and in side view, with the substrate located horizontally below the bubble (see the dashed line). The overall bubble dynamics is probably best perceived in side view.

Both time series are presented normalized to the respective bubble lifetimes $T_{\mathrm{L}}$. For a bubble in an unbounded liquid, here water at atmospheric pressure, the lifetime can be estimated by two times the Rayleigh collapse time: $T_{\mathrm{L}}^{\mathrm{th}} = 0.183\ R_{\max}$. For the derivation, an empty bubble, a collapse to zero size, and the same duration of expansion and collapse phase are assumed. The proximity to the solid boundary delays the collapse by a factor of $(1 + \frac{0.205}{\gamma})$ [15,47] and experimentally confirmed by Vogel and Lauterborn [25]. From the theoretical prediction one expects $T_{\mathrm{L}}^{\mathrm{th}}(\gamma = 1.21) = 88.6\,\mu\mathrm{s}$ and $T_{\mathrm{L}}^{\mathrm{th}}(\gamma = 1.42) = 86.7\,\mu\mathrm{s}$. That is in good agreement with the measured lifetimes of $T_{\mathrm{L}}(\gamma{=}1.21) = 85\,\mu\mathrm{s}\ (\pm 1.6\,\mu\mathrm{s})$ and $T_{\mathrm{L}}(\gamma{=}1.42) = 83\,\mu\mathrm{s}\ (\pm 1.6\,\mu\mathrm{s})$.

The bubble generated at $\gamma = 1.21$ (left) reaches its maximum expansion of $R_{\max} = 414\,\mu\mathrm{m}$ about $33\,\mu\mathrm{s}$ ($\tau = 0.39$) after seeding. The bubble is of quite spherical shape, only a minor deformation at the south pole due to the solid boundary is present (seen only in side view). With "south pole" we will always refer to the lower pole of the bubble in an image, and correspondingly the "north pole" is the pole appearing in the upper part of a figure. The bubble collapses between $\tau = 0.93$ and 1.00 ($t = 79\,\mu\mathrm{s}$ and $t = 85\,\mu\mathrm{s}$) close to the substrate into a toroidal shape which is well captured in the bottom view. The collapse is accompanied by a jet formation (see for example the indentation in side view at the north pole of the bubble and in bottom view the inner circle due to light diffraction by the changed curvature of the gas phase at $\tau = 0.93$). Between $\tau = 1.00$ and 1.46 ($85\,\mu\mathrm{s}$ and $124\,\mu\mathrm{s}$) the bubble rebounds, i.e., it reexpands along the substrate in a flat shape. Thereby, the gas phase interface exhibits a rugged boundary. During rebound around the axis of symmetry, secondary cavitation occurs, see the protrusion in side view above the flat shaped bubble. It is produced by shock waves emitted during the bubble collapse. This phenomenon has been termed "counter jet" (see Refs. [12,13,28]), even though there is no jet flow involved (as here definitely proved in Sec. IV). Instead, the secondary cavitation is stationary and does not move until being carried away by the vortex later (at $\tau = 2.84$).

Around $\tau = 1.46$ ($t = 124\,\mu\mathrm{s}$), the gas phase has reached the maximum rebound expansion and begins to collapse again. The second collapse occurs around $\tau = 1.79$ and again results in a toroidal shaped bubble. Around $\tau = 1.92$ only remnant bubbles which may still show moderate oscillations are left. They are detached from the substrate and migrate with a ring vortex in a perpendicular angle away from the substrate into the bulk liquid. We call this ring vortex, according to its migration direction into the bulk: "free vortex." The migration of the free vortex vertically upward can be well followed in the side view for $\tau \geqslant 1.92$. At the last frame ($\tau = 5.31$) the free vortex has travelled about $675\,\mu\mathrm{m}$ away from the substrate to the center of the image (side view). The free vortex can continue for several microseconds and migrate over a centimeter—that is more than 25 $R_{\max}$—through the bulk liquid.

The bubble generated at $\gamma = 1.42$ (right columns in Fig. 3), up to the first collapse at $t = 83\,\mu\mathrm{s}$ ($\tau = 1.00$) shows similar dynamics as compared to the previous case. Shape and size of the bubble at toroidal collapse are almost identical (bottom view at $\tau = 1.00$), except that the collapse takes part farther away from the substrate (compare both side views at $\tau = 1.00$). At $\tau = 1.07$, in side view, the gas phase shows a peculiar shape: a tip from the secondary cavitation ("counter jet") at the north pole, a bellied extension at the center of the gas phase from the re-expansion of the bubble, and a smaller contact of the gas phase with the substrate at the south pole, where the jet impinges through the gas phase on the solid. At $\tau = 1.46$, the maximum rebound extension is reached and at $\tau = 1.79$ the bubble collapses for a second time into a toroidal shape. After $\tau = 1.79$, a ring vortex that traps the remnant bubbles is seen to stretch radially (annularly) over the solid. In distinction to the free vortex we call this ring vortex the "wall vortex." Likewise, the free vortex persists for several microseconds before it disintegrates.

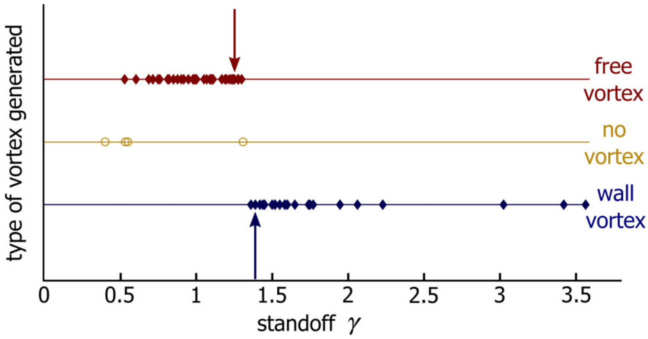

FIG. 4. Type of vortex ring generated by a collapsing bubble in dependence on the normalized standoff distance $\gamma$: Each data point on the upper line indicates the observation of a "free vortex" that is encountered in the range $0.5 \leqslant \gamma \leqslant 1.30$. The "wall vortex" (data points on the lower line) is observed for $\gamma \geqslant 1.36$. A very sharp transition between the two flow patterns is present. Only at some intermediate distance ($1.30 < \gamma < 1.36$), and for very small standoffs ($\gamma \lesssim 0.5$), no vortex ring seems to be created as no directed motion of the bubble fragments is observed. Instead bubble fragments rather "float" around the collapse location (data points on middle line). Maximum bubble radii ranged from $R_{\max} = 300\,\mu$m to about $450\,\mu$m. For the two observations indicated by the arrows, high-speed imaging series of the gas phase dynamics are given in Fig. 3.

While the remnant bubbles entrained in the vortex spread radially outward with the vortex, the bubble fragments generated as secondary cavitation stay around their origin of generation at the axis of symmetry, suggesting the absence of further flows.

A comparison of the time series of the two bubble shapes shows almost identical dynamics up to the first collapse. Thereafter, despite the fact that the bubbles were generated at only slightly different standoffs, they exhibit very different dynamics. Apparently, this is related to the diameter of the toroidally collapsed bubble ($\tau = 1.79$): At $\gamma = 1.42$, the inner torus radius amounts to more than double of the inner torus radius at $\gamma = 1.21$. Thus, at the second collapse, the bubble generated closer to the substrate rather collapses from its peripherals, while the bubble generated farther away collapses at first and dominantly from its symmetry axis. The ring vortices that emerge thereafter, are of opposite translation direction becoming visible by the remnant bubbles. In Sec. IV, the question how the motion of gas phase relates to the flow field will be answered.

The extent of gas phase contact to the wall is considered important for many applications such as surface cleaning. Thus, it is worth noting that the largest radial extension of the gas phase over the surface in the case of the free vortex is reached during the first rebound ($\tau \cong 1.46$), in the case of the wall vortex much later, during the radial stretching of the vortex ($\tau > 2.84$), where the vortex ring radius at vortex disintegration is larger than $R_{\max}$. For a systematic measurement of the contact of the gas phase and the torus radii at the second toroidal collapse as a function of the standoff; see Ref. [29].

### B. Free and wall vortex generation: a function of the standoff $\gamma$

In the previous section it was shown by high-speed imaging series that upon bubble collapse, either a free vortex or a wall vortex is generated. To determine the dependence of the vortex direction on $\gamma$, over 50 bubbles are generated at different standoffs and the direction of vortex migration is tracked by optical imaging of the remnant bubbles, as in Fig. 3. For a maximum accuracy, only spherically seeded bubbles are considered. Then, the dynamics and generated flow patterns are strikingly repeatable.

Figure 4 shows the type of generated vortex ring, each marker on the upper line denotes the observation of a free vortex and each marker on the lower line the observation of a wall vortex. It follows that in the range of $\approx 0.5 \leqslant \gamma \leqslant 1.30$ a free vortex and for $\gamma \geqslant 1.36$ a wall vortex is generated. The two regimes are divided by a very sharp and repeatable transition at a $\gamma$-value between 1.30 and 1.36. Within this narrow interval of the standoff parameter, flows seem to cancel out each other, the liquid comes to rest quickly, and no ring vortex at all is observed. A similar situation is found for $\gamma \cong 0.45$, where also no vortices are observed. However, a precise investigation of the parameter range $\gamma < 0.4$ is prevented by the current experimental technique putting some limitations on the generation of perfectly spherical bubbles generated too close to the substrate. In Video 1 of the Supplemental Material [48], additionally the shape dynamics of bubble collapsing without producing a vortex is presented (for $\gamma = 1.31$).

From the shape dynamics, a good overview of the bubble dynamics and the consequent ring vortex behavior is obtained. However, without the knowledge of the flow field surrounding the bubble many aspects stay unclear. Therefore, and with a particular focus on revealing the process of vortex formation, the full unsteady flow fields are presented and analyzed in the next section (Sec. IV) for a representative example of each the free and the wall vortex.

## IV. TIME-RESOLVED FLOW FIELDS

Quantitative knowledge about the cavitation-induced flow fields may not only be important for many applications but is also of fundamental interest and allows us here to investigate the formation mechanisms of the two types of ring vortices presented in the previous section. So far, insights into the cavitation-induced flows, especially into the flows after the jet impact on the substrate, are fragmentary. Particle velocimetry techniques, capable of the measurement of the full flow field, have been applied before only to bubbles confined in two dimensions [49], which have quite different characteristics than the bubbles commonly generated by ultrasonic cavitation, or to quite large collapsing bubbles as in the works by Vogel *et al.* [28] and Kröninger *et al.* [45]. Their bubbles measured about 2.5 to 5.0 mm in diameter. In ultrasonic applications, however, active bubbles can be expected to be of smaller size, for example, the (linearized) resonant diameter of a bubble at 25 kHz driving amounts to 120 $\mu$m [50]. Especially because flows in the near-wall region are of interest, viscous effects may play a different role. Here, for full flow field data retrieval, we applied a $\mu$PIV/PTV technique to bubbles of about 325 $\mu$m diameter (at maximum expansion), thus five- to tenfold smaller than in previous works and comparable to the size of ultrasonically induced bubbles, which in turn poses increasing demands on the experimental technique, as not only the geometry is reduced by five to ten times but also the time scale of the bubble dynamics.

In this section, the shape dynamics are related to the interacting fluid flow field. Long-term time series of the velocity fields produced by aspherically collapsing bubbles are presented together with the simultaneously recorded gas shape dynamics for a bubble generating a free vortex (Sec. IV A) and for a bubble generating a wall vortex (Sec. IV B). As we operate our imaging equipment at the current technical limits, for each vortex type two flow field time series need to be presented. One covers the “entire” spatial surrounding of the bubble at a moderate high-speed imaging rate (40 000 fps), thereby offering an overview of the whole dynamics. The second one focuses on a smaller geometric section containing only the substrate and where the region of vortex generation, in turn allowing for a higher temporal resolution (imaging frequency 135 000 fps). In Sec. IV C a detailed and quantitative analysis of the ring vortices is made.

### A. Free vortex

In Fig. 5, the evolution of the velocity field generated by a collapsing bubble is shown for eight subsequent times (read from left to right and top to bottom). The times, with respect to the bubble generation, are indicated in the top left corner of each frame in absolute and normalized form. The velocity field is determined from particle imaging with interframe time $\Delta T_{\mathrm{PIV}} = 25\,\mu$s (40 000 fps) and exposure time $\Delta T^{\mathrm{e}}_{\mathrm{PIV}} = 20\,\mu$s. This means that the velocity is averaged over 25 $\mu$s and the times indicated in the frames are quoted as the center of the 25 $\mu$s-exposure interval, for example the first frame ($t = 51\,\mu$s) reflects the fluid flow in the time interval [38.5 $\mu$s ... 63.5 $\mu$s]. Simultaneously

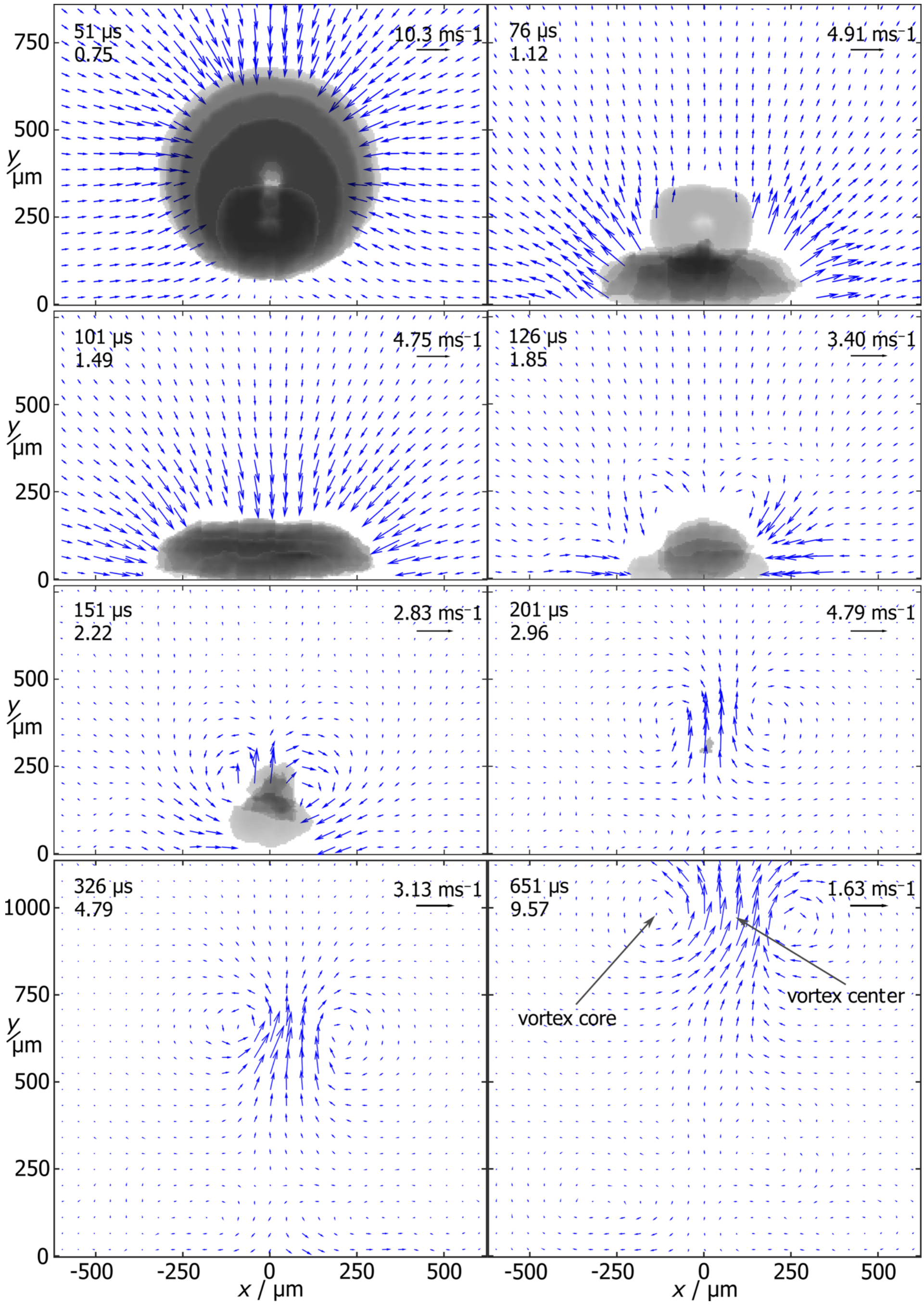

FIG. 5. Time evolution of the velocity field of a free vortex generated by a collapsing bubble ($\gamma = 1.21$; $T_L = 68\,\mu s$; $R_{\max} = 325\,\mu m$). The solid boundary extends along $y = 0$. Times indicated in the top left corner of each frame are given with respect to bubble seeding (at $t = 0\,\mu s$) in absolute values and in nondimensionalized form $\tau = t/T_L$.The motion and dynamics of the gas phase during the velocity measurement are overlaid up to the frame at $\tau = 2.96$, thereafter the gas is mainly dissolved. The local velocity is given by the arrow length, the respective scale for each frame is shown in the top right corner. Velocities are integrated over a time span of $\Delta T_{PIV} = 25\,\mu s$ around the times given ($\pm 12.5\,\mu s$).

to the exposure of the particle image, the shape of the gas phase is imaged by the bubble camera (interframe time $\Delta T_{\text{bub}} = 5.6\,\mu\text{s}$, $\sim$180 000 fps, exposure time $T^{\text{e}}_{\text{bub}} = 370\,\text{ns}$). The respective gas phase images are overlaid to the velocity field in Fig. 5. As $\Delta T_{\text{PIV}}$ is 4.5 times $\Delta T_{\text{bub}}$, about five gas shapes correspond to each velocity field.

The bubble shown is generated at $\gamma = 1.21$ and the maximum radius amounts to $R_{\text{max}} = 325\,\mu\text{m}$. The bubble collapses at $T_{\text{L}} = 68\,\mu\text{s}$ ($\tau = 1.00$) for the first and at $T_{\text{L2}} = 127\,\mu\text{s}$ ($\tau = 1.87$) for the second time. For $\tau > 2.96$, even the remnant bubbles have almost completely disappeared (and no further overlay of the gas phase is made). The dynamics shown in Fig. 5 can be roughly divided into four stages: (1) bubble collapse and jet formation ($\tau = 0.75$); (2) rebound at the substrate ($\tau = 1.12$); (3) second collapse ($\tau = 1.49$, now taking part at the substrate); (4) ring vortex formation and propagation ($\tau \geqslant 1.85$).

Now a more detailed discussion of the induced flows is made. At the frame $\tau = 0.75$, the bubble is on the point of collapsing from its maximum expansion. Thereby the bubble centroid migrates toward the substrate. Between bubble and substrate, a stagnation area develops (from about $x = -100\,\mu\text{m}$ to $100\,\mu\text{m}$). Around the northern bubble hemisphere, an about radial velocity field is present. It has higher flow velocities closer to the axis of radial symmetry. This is a result of the jet that pierces through the bubble's north pole toward the substrate. In the next frame ($\tau = 1.12$) the bubble impacts on the substrate where it rebounds with a rugged phase boundary. From the jet impact on the substrate, an annular flow away from the axis of symmetry over the substrate appears and liquid is ejected from the near-wall layer. This is the stage of bubble dynamics when most kinetic energy has been transferred to the liquid close to the substrate. The kinetic energy in the liquid is derived from the flow field as $E_{\text{kin}} \cong 1.2\,\mu\text{J}$ and can be compared to an estimation of the bubble energy. The volume work $E_{\text{V}}$ against atmospheric pressure $p_{\text{a}}$ stored with the expanded bubble yields $E_{\text{V}} = \frac{4}{3}\pi R^3_{\text{max}} p_{\text{a}} = 14.4\,\mu\text{J}$. Thus, the observed $E_{\text{kin}} \cong 8\% E_{\text{V}}$ is in agreement with the expectation that 80–95% of the bubble energy is radiated by shock wave emission [25,30]. Still, $E_{\text{kin}}$ (being proportional to $v^2$) may be underestimated experimentally due to unavoidable temporal and spatial averaging, in particular when the kinetic energy is concentrated on a small liquid volume, for example by the jet.

At $\tau = 1.49$ the jet flow from the first collapse has ceased and the liquid follows the collapse of the pancake-shaped bubble on the substrate. A second jetlike flow that pierces the bubble at the axis of symmetry builds up, while at the same time a similarly intense flow along the substrate follows the inward collapsing bubble wall toward the axis of rotational symmetry ("annular jet"). Between the rebound at the substrate ($\tau = 1.12$) and the subsequent collapse ($\tau = 1.49$) the overall direction of flow changes abruptly. The change in liquid momentum in vertical direction $\Delta p_y$ associated with this flow direction change must be transferred to the substrate, mainly during jet impact. Assuming again the rotational symmetry of the flow field, we obtain as a lower bound for the momentum transfer: $\Delta p_y = 7 \times 10^{-8}\,\text{kg}\,\text{ms}^{-1}$.

At $\tau = 1.85$, a peculiar flow pattern similar to a heart shape is visible and apparently significant circulation is introduced into the liquid. The gas phase detaches from the wall, while there is still an annular flow over the substrate toward the axis of symmetry present (annular jet). At $\tau = 2.22$ the remnant bubbles are moving further upward, vertically away from the substrate, and a ring vortex is developing (seen here in 2D cross section). At $\tau = 2.96$, the free ring vortex is fully developed. So far it has moved approximately $360\,\mu\text{m}$ off the substrate. The maximum (vertical) flow velocities are found around the (confined) vortex ring center (the inner vortex diameter measures around $180\,\mu\text{m}$) and reach up to $v_y = 4.8\,\text{ms}^{-1}$. In the further course (compare to the last frame, $\tau = 9.57$), the vortex continues to migrate away from the wall while gradually the translation velocity and maximum flow velocity in the free vortex decrease. Then the free vortex broadens as vorticity diffuses throughout the liquid. By diffusion of vorticity and momentum, the vortex radius stretches, the vortex size increases. As thereby more liquid is entrained into the vortex, the translation velocity decreases in consequence of conservation of momentum. The $y$-coordinate of the vortex trajectory $y_v(t)$—the distance the vortex core has travelled away from the wall—is shown in Fig. 6. For a quantitative analysis of the vortex, its circulation and vorticity see Sec. IV C.

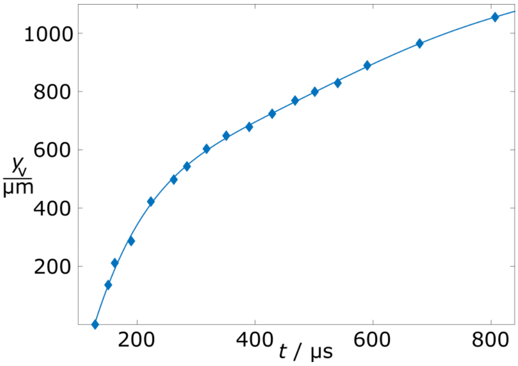

FIG. 6. Trajectory of the free ring vortex, characterized by the travelled vertical distance $y_v$ over time. For later use of the translation velocity, a polynomial fit (solid line) is shown.

Figure 5 demonstrated an overview of the unsteady flow field of the entire bubble surrounding. However, the very details of the vortex formation are too fast to be completely resolved at the imaging rate of 40 000 fps. Therefore, in Fig. 7 the flow field time series from a repeated experiment is presented but captured at a higher temporal resolution being now 135 000 fps. Note that for a compact representation, the frame sequence for the large geometrical image section run from left to right and then top to bottom (Fig. 5), whereas now, for the very high temporal sampling in Fig. 7, it runs first from top to bottom, then from left to right. At this frame rate only a smaller geometric section can be imaged, for this reason the y-axis extends only to about 400 $\mu$m now. Since the bubble shape is recorded at 250 000 fps, to every flow field plot, three gas shape images are overlaid. Again, the time series can be divided into different stages: (1) first collapse ($\tau = 0.87 \ldots 0.97$); (2) rebound phase on the substrate ($\tau = 1.07 \ldots 1.36$); (3) second collapse phase on the substrate ($\tau = 1.36 \ldots 1.75$) with toroidal collapse around $\tau = 1.76$; (4) ring vortex formation and propagation ($\tau \geqslant 1.75$). Note that after the second collapse only remnant bubbles are left—they may oscillate in a coupled manner—and images overlaid at times larger than $\tau = 1.75$ are rather a result of the cloud of gas fragments than of one gas entity.

In the faster time series larger maxima of the flow velocity are resolved and some more details become apparent. In the moment of collapse (covered by the image at $\tau = 0.97$) the maximum resolved velocity associated with the jet impinging at the bubble north pole is now over 17 ms$^{-1}$. In addition to the downward jet, intense sideways flows toward the axis of symmetry and following the translating bubble are visible (see at $y \cong 150\,\mu$m, note that the velocity vector scale is 17.6 ms$^{-1}$). In the next time step, together with the jet flow that now extends annularly after its impact on the substrate, the bubble explosively reexpands along the substrate into a flat shape. At $\tau = 1.36$ the flow field reflects an intriguing phase of the bubble dynamics. The bubble is transforming into a toroidal shape—it cannot be perceived in this side view projection, but it can in Fig. 3 (leftmost column, bottom view). While the gas phase on the outer torus boundary is still expanding, the bubble already begins to collapse from the inner torus boundary again forming an axial jet. This causes a flow between the regions of expanding and collapsing gas phase along a semi-circle that feeds the axial jet. The next two frames ($\tau = 1.56$ and $\tau = 1.65$) show the second collapse phase. Intense flows that converge toward the point where the axis of radial symmetry intersects the boundary appear. As the second collapse proceeds, converging flows collide ($\tau = 1.75$). This results in high shear in the liquid and in consequence a complex, turbulent scenario develops where the structure of the flow field gets locally three-dimensional (and the assumption of radial symmetry may no longer be valid). The second collapse may be considered as the starting point of ring vortex formation. In the following frames, the ring vortex takes further shape still in the vicinity of the substrate. Then the vortex lifts off and migrates together with the remnant bubbles perpendicularly away from

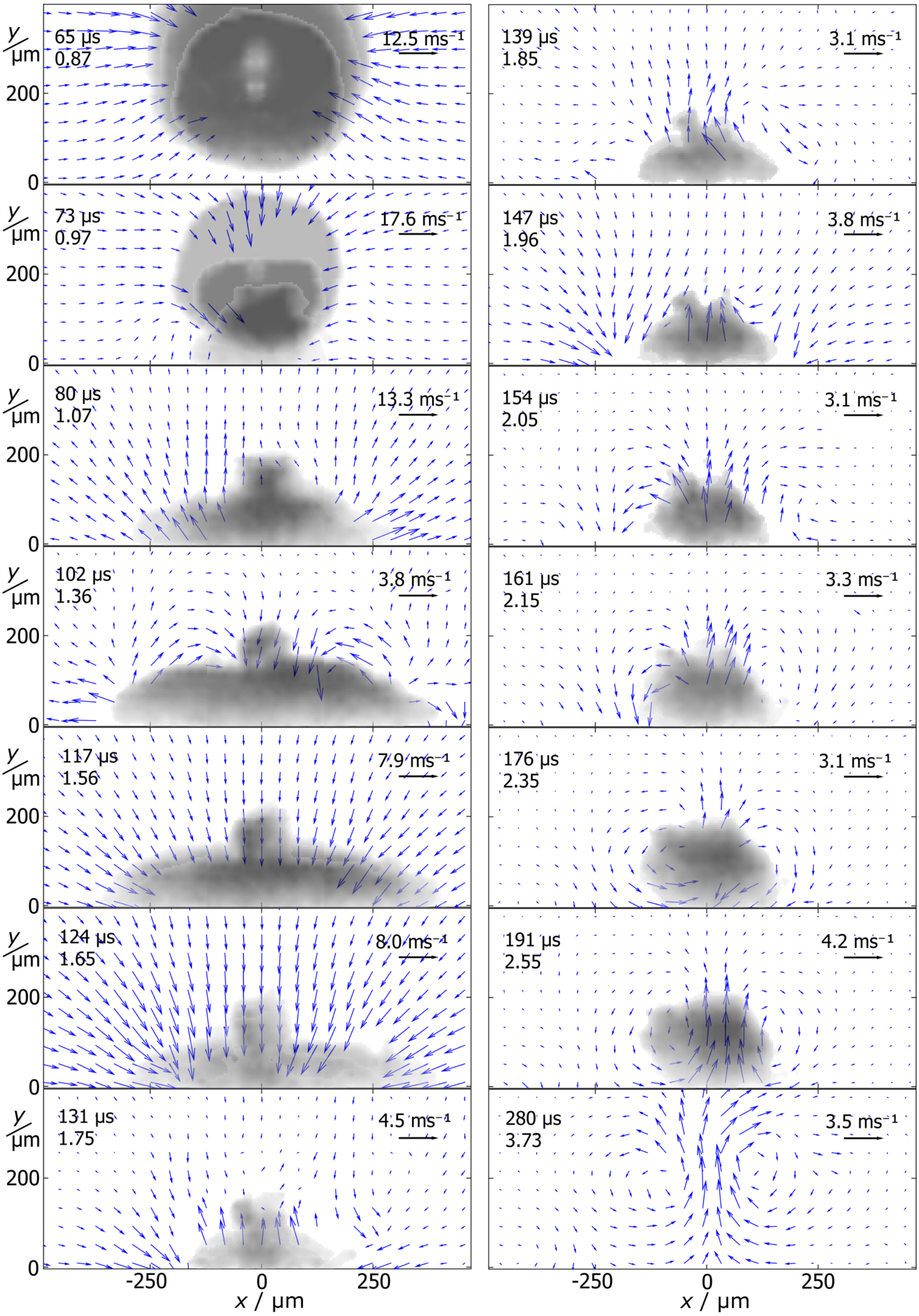

FIG. 7. Time evolution of the velocity field of a bubble generating a free vortex, situation similar to Fig. 5 but captured at a higher frame rate of 135 000 fps ($\gamma = 1.1$; $R_{\max} = 340\,\mu$m; $T_{\mathrm{L}} = 75\,\mu$s; $T_{\mathrm{L2}} = 131\,\mu\mathrm{s} - T_{\mathrm{L}} = 56\,\mu$s). The time elapsed since bubble generation is indicated in absolute values and normalized to $T_{\mathrm{L}}$. Frames proceed column-wise. $\Delta T_{\mathrm{PIV}} = 7.4\,\mu$s, $T^{\mathrm{e}}_{\mathrm{PIV}} = 5.5\,\mu$s.

the substrate. Thereby, it repeatedly loses and gains some momentum from subsequent oscillations (after-bounces) of the remnant bubble cloud. Hence the generation of the free vortex ring can be attributed to the collapse of the flattened toroidal bubble in the boundary layer at the substrate that occurs predominantly annularly in the boundary layer at the wall.

In particular, for ultrasonic surface cleaning applications the flow velocities close to the substrate and especially the wall shear rates are of great relevance. Here the wall shear rate $\dot{g}$ is approximated by $\dot{g} = \frac{v_x(\Delta y)}{\Delta y}$ assuming a linear velocity profile which (also due to the time-averaging over $\Delta T_{\mathrm{PIV}}$) provides a lower boundary for the wall shear rate.

The highest velocities at the substrate are generated during rebound ($\tau = 1.07$) and during toroidal collapse at the substrate ($\tau = 1.65$). The maximum wall shear rate that covers a significant substrate surface is only produced along with the toroidal collapse of the bubble ($\tau = 1.65$). During rebound velocities are high as the axial jet and the gas phase that reexpands at the substrate work together to eject liquid from the boundary layer as can be seen by the vertical component of the flow velocity (that however does not contribute to the wall shear rates). In the case of the second toroidal collapse, as the pancake-shaped bubble collapses at the substrate from the periphery, flows are directly produced along and parallel to the substrate surface. Thereby, the wall shear generated is more important. Rates of $\dot{g} = 5 \times 10^5 \mathrm{s}^{-1}$ are still reached even at a larger radial distance from the symmetry axis up to about $x = R_{\max}$.

### B. Wall vortex

Now the flow field of a bubble generating a wall vortex is discussed. Again, first an overview of the flow field is given (Fig. 8), and then more details are discussed along with a time series of the highest temporal resolution (Fig. 9).

Read Fig. 8 from left to right and top to bottom. In the first frame ($\tau = 0.30$) the bubble is in the expansion phase whereby it established a radial velocity field especially around the northern bubble hemisphere. Visibly, the velocity field in the southern bubble hemisphere is distorted by the presence of the solid boundary. In particular, directly below the bubble a stagnation area at the substrate has developed. In the next frame ($\tau = 0.69$) the bubble starts to collapse and there is a radial velocity field of reversed direction. It is now much more pronounced around the northern hemisphere related to the axial jet that is going to pierce through the bubble north pole. Consequently, the bubble is compressed in such way that it translates toward the solid boundary as the momentum of the flow pointing toward the substrate (from around the northern hemisphere) overweighs the momentum of the flow pointing away from the substrate (from around the southern hemisphere).

Within the timespan of the subsequent frame, the bubble collapses (at $T_{\mathrm{L}} = 61\,\mu\mathrm{s}$) and rebounds. The translatory motion toward the substrate is accelerated (seeding was at $y = 510\,\mu\mathrm{m}$, collapse is around $y = 260\,\mu\mathrm{m}$). This is connected to respective liquid displacement and annular liquid ejection, part of which upward, away from the axis of symmetry. The frame at $\tau = 1.52$ mainly images the course of the second collapse. A second jet is building up with measured velocities up to $6.8\,\mathrm{ms}^{-1}$ but in fact surely being faster in the bubble interior which cannot be imaged.

At the next frame ($\tau = 1.93$) the velocity field shows a remarkable pattern. While still a remnant (axial) jet flow toward the substrate is present, there is also an annular flow toward the bubble centroid. It is generated directly at the substrate, passing along the substrate by the toroidal collapse commencing from the outer torus phase boundary. This type of flow we denote as "annular bubble collapse." Here we identify the annular bubble collapse at the substrate as an important mechanism for the generation of high wall shear rates. Note that the inflow from north-east and north-west directions is much slower.

At $\tau = 2.34$, the gas phase—from these images it seems to extend all the way along the substrate, but it actually has a toroidal shape (as seen in Fig. 3, right column, bottom view)—further collapses and a thicker axial jet (width about $180\,\mu\mathrm{m}$) impacts on the substrate. At the same time, liquid from the near-wall layer at more peripheral positions ($|x| \cong 350\,\mu\mathrm{m}$) is fed back into the jet along (semi-)circular streamlines.

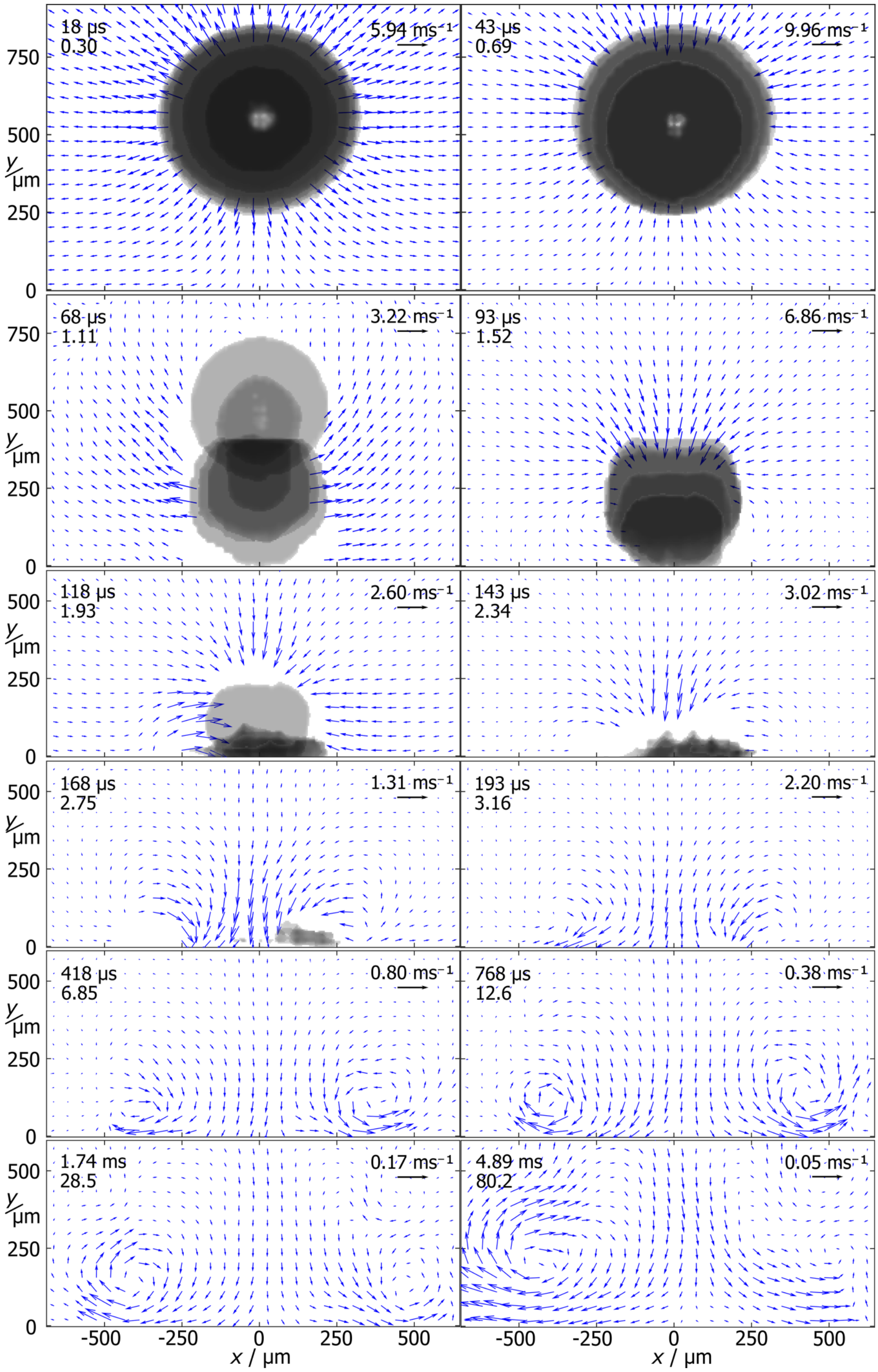

FIG. 8. Time evolution of the velocity field of a wall vortex (the solid boundary extends along $y = 0$) generated by a collapsing bubble ($\gamma = 1.67$; $T_L = 61\,\mu$s; $R_{max} = 310\,\mu$m). The motion and dynamics of the gas phase during the velocity measurement are overlaid up to $\tau = 2.75$, thereafter the gas is mainly dissolved. Times indicated in the frames are given with respect to bubble seeding (at $t = 0\,\mu$s). Time sequence row-wise. Velocities are integrated over a time span of 25 $\mu$s around the times given.

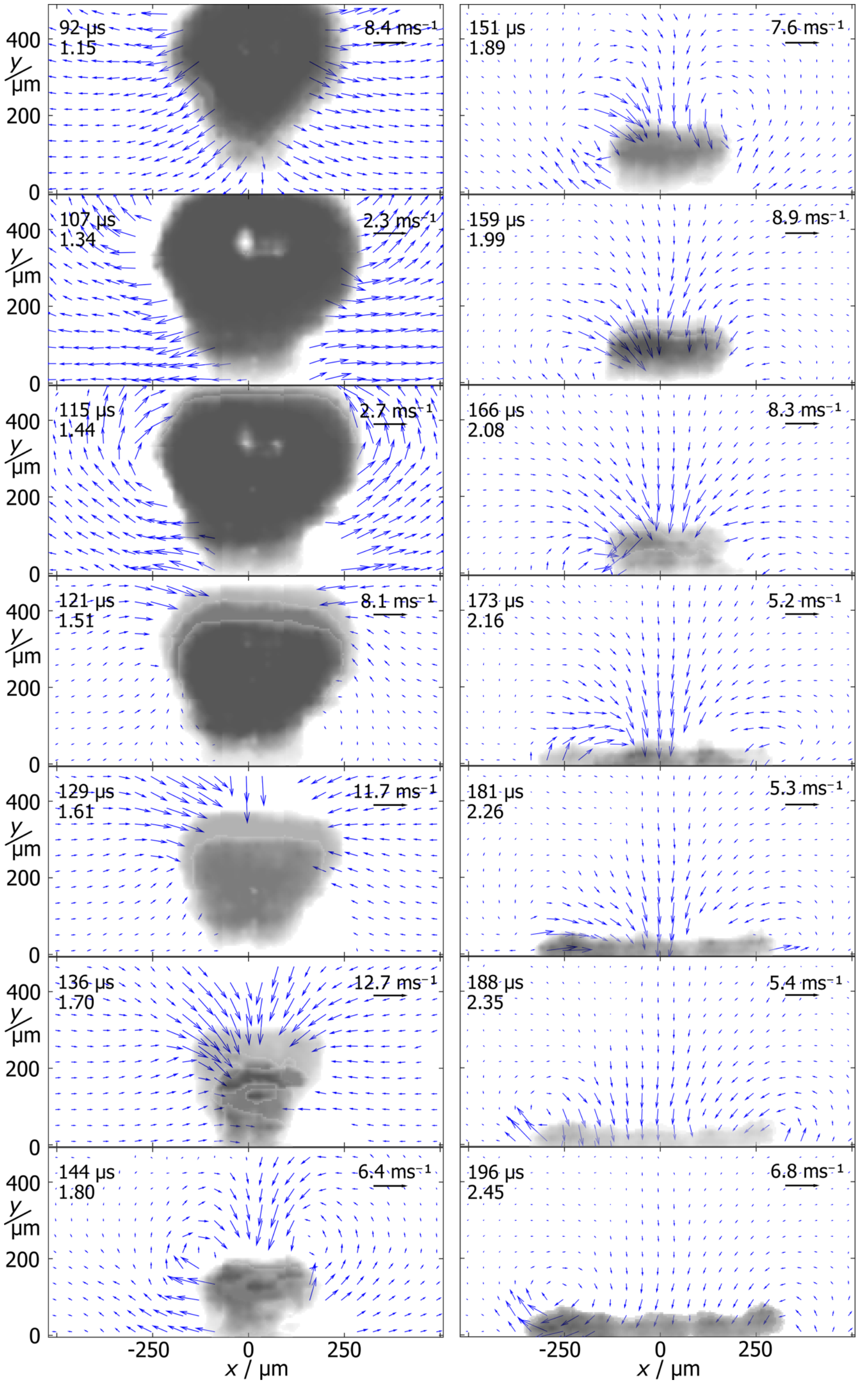

FIG. 9. Time evolution of the velocity field of a bubble generating a wall vortex resolved at 135 000 Hz ($\gamma = 1.75$, $T_L = 80\,\mu$s, $R_{\max} = 420\,\mu$m). At $t = 115\,\mu$s already a circular flow pattern is visible. Then between $t = 136\,\mu$s and $144\,\mu$s the wall vortex has clearly emerged at about $y = 200\,\mu$m. Times $t$ and $\tau$ of frames are given in top left corner in microseconds and normalized form below. Frames proceed from top to bottom and then left to right.

At the two later times ($\tau = 2.75$ and $\tau = 3.16$), the formation of a ring vortex (sliced by the imaging plane of the velocity field) is manifesting and in the further course the ring stretches radially along the substrate. The vortex motion is geometrically and viscously damped, thus the vortex slows down and the vortex slowly lifts off the substrate (compare the vortex core positions in the last four frames).

Now the key frames of vortex formation and dynamics are analyzed at a higher temporal resolution of 135 000 Hz; see Fig. 9 (read the figure now from top to bottom and left to right).

The first frames ($\tau = 1.15-1.44$) cover the rebound phase. Thereby, the bubble displaces liquid sideways. As the bubble is pierced by the jet it has acquired an elongated shape. The jet impacts on the substrate between $\tau = 1.15$ and 1.44 and subsequently proceeds annularly along the substrate. At $\tau = 1.44$ for the first time a circular flow pattern clearly emerges. As the bubble moves toward the substrate, it first collapses preferably from the north pole forming a second axial jet ($\tau = 1.51$ and 1.61) and then it collapses annularly (see the secondary flow toward the axis of symmetry at $|y| \cong 180\,\mu$m). At $\tau = 1.70$ the bubble is completely punctured by the axial jet and subsequently collapses into a toroidal shape about 180 $\mu$m away from the substrate.

At the next time step ($\tau = 1.80$), the ring vortex has formed and appears as a distinct structure in the flow pattern. It is an important observation that the ring vortex is generated with its center being located at $y = 200\,\mu$m. Thus, it is not generated where the jet pierces through the bubble or impacts onto the substrate, neither where splashing is expected to occur, but with the vortex core coinciding with the location of the gas phase during the toroidal collapse. So, the vortical flow circulates around the remaining "ring" of extremely compressed gas. In addition to the emerged ring vortex, the jet is still spreading over the substrate being fed by further liquid at its wake, which apparently contributes to a further vortex manifestation. The next time steps ($\tau = 1.89$–2.35) illustrate how the wall vortex migrates toward the substrate. The presence of the solid boundary distorts the vortex. Still some secondary flows from weaker after-bounces of the remnant bubbles are contributing to the flow field. However, from $\tau \cong 2.0$ the gas phase is completely fragmented and there are only unconnected remnant bubbles left. The last three frames, at times $t = 2.26$–2.45, show the radial expansion of the vortex along the surface.

The highest wall shear rates are measured not before the second collapse but for $\tau \geqslant 1.70$. Thus, when the gas phase has moved toward the solid and the bubble dynamics take place close to and, due to the flattened shape, along the substrate. Wall shear rates of $\dot{g} > 3 \times 10^5\ \mathrm{s}^{-1}$ are exerted by annular flows of similar magnitude toward the axis of symmetry (for $\tau = 1.70$, and $\tau = 2.26$) as well as away from the axis of symmetry (for $\tau = 1.80$, and $\tau \geqslant 2.35$). The flows exhibiting the highest wall shear rates directed toward the axis of symmetry are generated during the second and third collapse respectively and follow the collapsing bubble wall. The flows directed away from the axis of symmetry exhibiting high wall shear result in the first case ($\tau = 1.80$) from the axial jet after its impact on the substrate working together with the expanding gas phase. It should be mentioned here that within the gas phase in a very thin layer intense liquid flows may be present from the jet impact on the substrate, but they may not be resolved here. For $\tau \geqslant 2.35$ the highest wall shear rates are exerted by the vortex. The maximum is located always where the vortex core traverses the substrate. By radial stretching of the vortex significant wall shear rates are exerted along a larger area. But as the vortex gets geometrically damped, shear rates decline as the distance from the axis of symmetry increases, for example to $\dot{g} = 9 \times 10^4\ \mathrm{s}^{-1}$ at $\tau = 4.0$ at $x = R_{\mathrm{max}}$.

### C. Quantitative analysis of the vortex

It is well known that an aspherical bubble collapse is associated with the introduction of vorticity into the liquid, and here we generally observe the formation of a distinct vortex ring that prevails for a time significantly longer than the bubble itself. Vortex rings have been widely studied in general context [51–54].

As the vortices here carry most of the momentum and circulation generated by the collapsing bubble, a further characterization and analysis is needed.

For the free vortex, we apply now an analytical model of a ring vortex in an unbounded liquid. Generally, a ring vortex is known to induce some self-propulsion and with the model we are going

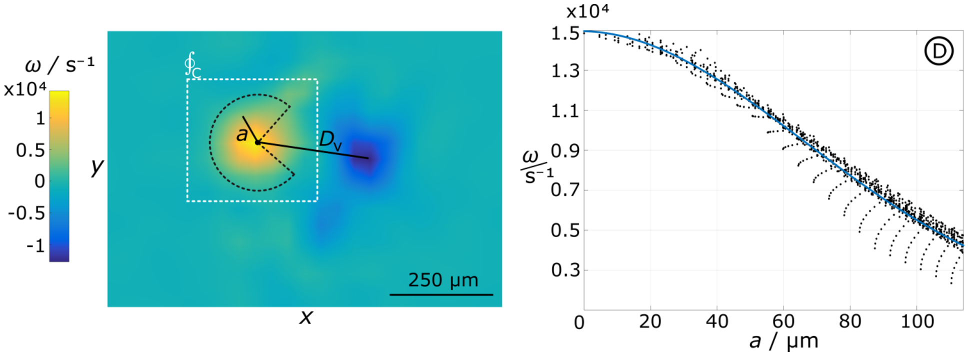

FIG. 10. Left: Color coded vorticity $\omega$ of the velocity field from the ring vortex of Fig. 5 (shown here at $t = 451\,\mu$s, $\gamma = 1.21$). The dashed white line depicts the path C of the integral that can be used to calculate the circulation. For more details on the determination of the circulation and vorticity see the Appendix C. The dashed black line depicts the circular sector within which the data points are considered for the Gaussian fit for the right image. The black lines indicate the radial coordinate $a$ and the ring vortex diameter $D_v$. Right: Measurement data of the vorticity (from the circular sector of the left graphic) with Gaussian fit around the vortex core.

to answer the question if there are more principles behind the translational motion of the free vortex. We adapt the approach from Saffman [55] and assume a Gaussian distribution of vorticity in the vortex core. Then $U_\Gamma$, the self-induced velocity of vortex translation, reads

$$U_\Gamma = \frac{\Gamma}{2\pi D_v}\left[\ln\frac{4D_v}{\sqrt{4\nu t_\Gamma}} - 0.558\right], \tag{1}$$

where $\nu = 1.00 \times 10^{-6}\,\mathrm{m^2 s^{-1}}$ is the kinematic viscosity of water and $t_\Gamma$ marks the virtual time when the ring was concentrated on a circle line which we take here as the time of the first collapse. Thus, in a given medium, the ring vortex is fully characterized by the size of its viscous core ($\sqrt{4\nu t_\Gamma}$), its circulation $\Gamma$ and its diameter $D_v$. The vortex diameter $D_v$ can be easily determined in a vorticity plot of the velocity field (vorticity $\omega = \frac{\partial v_y}{\partial x} - \frac{\partial v_x}{\partial y}$) as the distance between the location of minimum and maximum vorticity; see the color-coded vorticity plot in Fig. 10 (left).

The circulation is determined from the vorticity as described in Appendix C by fitting Gaussians of the form $\omega(a) = K\exp\left(\frac{a}{\sigma}\right)^2$ at the vortex core, where $a$ is the radial distance from the vortex core and $\sigma$ and $K$ are the fit parameters so that $\Gamma$ is given by $\pi K\sigma^2$. As the Gaussian profile is distorted on the inner side of the ring, the data points outside the circular section sketched in Fig. 10 (left) are excluded. In Fig. 10 (right) a vorticity profile $\omega(a)$ with a respective fit (at $t = 326\,\mu$s) is shown. The plot visually justifies the assumption of Gaussian vorticity profiles which holds for times later than $250\,\mu$s (all fits have a coefficient of determination $R^2 > 0.97$—a perfect fit would have a coefficient of determination of $R^2 = 1$). Only during vortex formation, the vorticity profile differs from the Gaussian model ($R^2 > 0.85$).

The Gaussian vorticity profiles taken at four times are plotted in Fig. 11 (left). The profile at the earliest time ($t = 151\,\mu$s) shows a very narrow vorticity distribution and the vortex is still in a process of formation—the vortex diameter is quite small and so is the circulation. In the respective velocity plot (Fig. 5 at $\tau = 2.22$) the presence of an annular jet that will merge with the vortex and that will "push" the vortex upward can be observed. For the three later times ($226\,\mu$s, $376\,\mu$s, $651\,\mu$s) attenuation of vorticity and progressive broadening of the profile are observable.

For completeness, the circulation $\Gamma(t)$ is shown in Fig. 11 (right). In Fig. 12 the corresponding self-induced velocity $U_\Gamma(t)$ according to Eq. (1) is compared to the measured velocity $U_y(t)$, which is calculated as the derivative of the fit to the vortex core $y$-positions (see Fig. 6). Actually, an exponential decay of vortex translation velocity for short times and a $1/t$ proportionality is expected

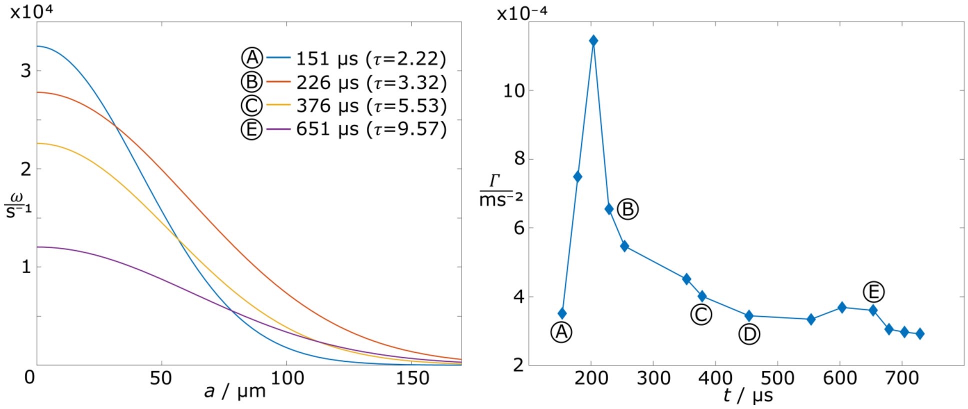

FIG. 11. Left: Gaussian vorticity profiles shown at four selected times (fits). Right: Time evolution of the circulation $\Gamma(t)$ of the free vortex (determined from the Gaussian vorticity profiles). The times A, B, C, E (see left figure), and D (see Fig. 10, right) for which the vorticity profiles are plotted are indicated.

[56]; however, here we employ a polynomial fit to the vortex positions as to include the formation process in vicinity to the solid boundary. The first three data points of $\Gamma$ (up to $t \cong 200\,\mu$s) still cover the process of vortex formation during which the circulation associated with the free vortex increases. For later times ($t > 200\,\mu$s), the ring vortex has fully evolved and both curves $U_\Gamma$ and $U_y$ agree very well. Thus, the ring vortex translation can be fully described by self-induced propulsion.

The circulation $\Gamma(t)$ of the wall vortex is shown in Fig. 13 (obtained from the path integral). Note, that the circulation of the wall and the free vortex are of similar magnitude. However, for the vortex stretching along the wall, damping effects are more pronounced. The flow field associated with the vortex is visibly distorted by the presence of the boundary and the vorticity is not rotational symmetric around the vortex core. To our knowledge, there is no analytical description of a viscous ring vortex stretching along a solid boundary. But here we can provide data for numerical simulations that could further elucidate the exerted wall shear forces.

## V. MIXING AND NET DISPLACEMENT OF FLUID BY A SINGLE COLLAPSING BUBBLE

In the previous sections shape dynamics (Sec. III) and flow fields (Sec. IV) were presented and analyzed to explore the mechanisms of flow generation by the collapsing bubble. Wall shear rates

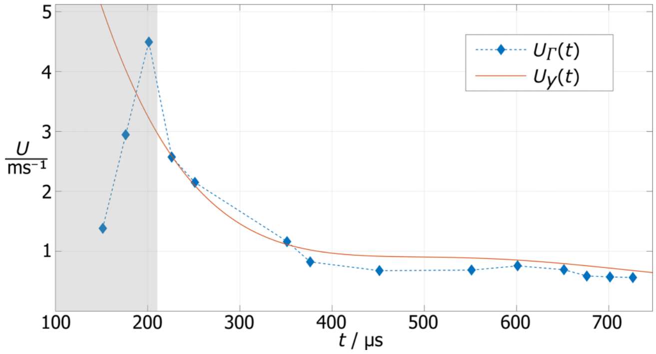

FIG. 12. Comparison of the self-induced ring vortex velocity $U_\Gamma(t)$ assuming Gaussian vorticity profiles (for $\gamma = 1.21$) compared to the measured velocity (the translation velocity of the vorticity maximum, derived from the fit of Fig. 6). Before $t \cong 210\,\mu$s the vortex is still in the stage of formation (masked space), thereafter the ring vortex has completely developed, and predicted translation velocity and measured velocity correspond well.

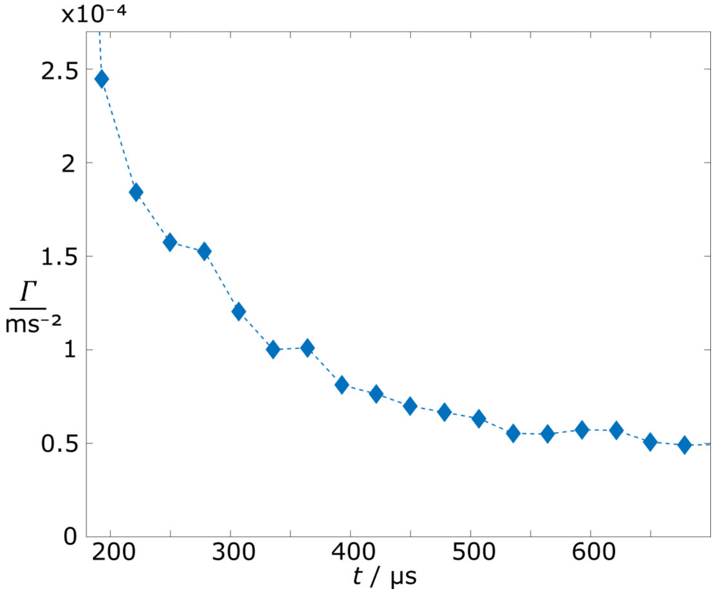

FIG. 13. Circulation $\Gamma(t)$ of the wall vortex of Fig. 8 (determined by the path integral).

and maximum velocities were deduced. They are particularly important for the estimation of surface cleaning and erosion. In this section, the net liquid displacement achieved by the bubble generated flows is analyzed being relevant for applications of acoustic and hydrodynamic cavitation, where it is intended to enhance mass transfer and accelerate diffusion limited processes. A typical goal in process and chemical engineering for example in mixing, sonochemical, or surface-coating processes (for sonochemical applications, see Refs. [57–59], for surface coating, see, for example, Refs. [60,61], and for mixing, see, for example, Refs. [62–64]). In general, mixing and mass transfer rely on similar physical mechanisms. In both cases, diffusion can only play a role on a very short length scale. For larger scales, strong process accelerations can be achieved by convection, shearing and stretching of fluid elements to increase the effective interfacial area between fluid elements, actually rendering many reaction processes industrially possible. In the present analysis we focus on mixing, but most aspects apply equally to any other mass transfer limited process assisted by cavitation.

The quantification and measurement of mixing, in general, is subject of current research. Common experimental techniques used for systems involving cavitation include the measurement of acceleration of a chemical reaction (by ultrasound-induced mass transfer enhancement), the balance between competing reactions (such as the Villermaux-Dushman protocol; see, for example, Ref. [65]) or the imaging of mixing of dyed fluids, which, however, has the disadvantage of averaging over the entire optical path. Furthermore, velocimetry techniques, such as PIV or PTV, are applied (for a review, see Ref. [66]). However, ultrasonic systems put some limitations to the applicability of the aforementioned techniques. Bubble structures obscure the view on the flow field and the sonicated liquid typically heats up, interfering with measurements of chemical reaction rates. Therefore, velocimetry techniques have been mainly applied to acoustic streaming and not to the microconvection generated by cavitation bubbles so far.

Here—dealing with unsteady flows—we want to give another perspective on mixing and portray the net displacement of liquid to elucidate mechanisms and the potential of micromixing by single collapsing bubbles. Therefore, we calculate the net displacement from the full velocity field of the $\mu$PIV/PTV-data by a Lagrangian approach tracking fluid particles along the unsteady flow fields. Therefore, each fluid particle is "ink-labelled" dark blue for fluid particles starting at the substrate, and lighter green to white colors for fluid particles starting at locations more remote from the

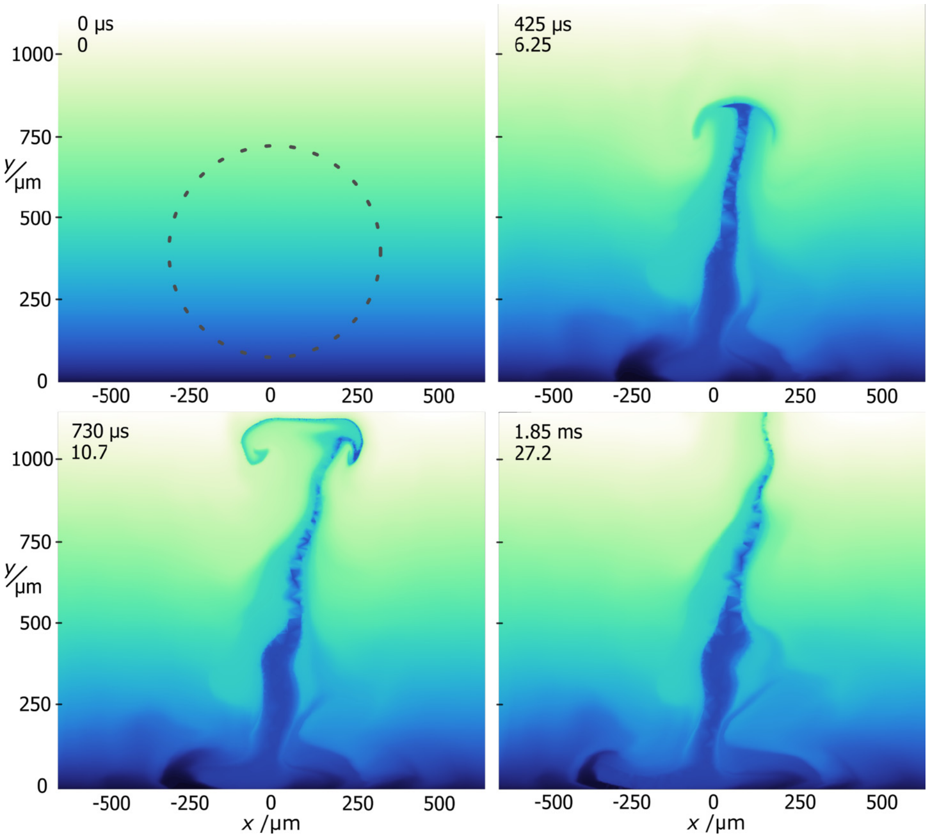

FIG. 14. Lagrangian ink map of a free vortex derived from the time-resolved flow field that was obtained experimentally by $\mu$PIV/PTV. The bubble is generated at $\gamma = 1.21$ ($t = 0$), the boundary extends horizontally along $y = 0$. Absolute times $t$ and nondimensionalized times $\tau$ are given in each frame. In the first image ($t = 0$) the initial ink configuration is shown: horizontal, colored layers from white (top) to dark blue (bottom). Also, the bubble shape at its maximum expansion is depicted (the maximum expansion is reached later, at $t = 34\,\mu$s). Along with the formation and migration of the free vortex ring, liquid is ejected from the boundary layer into the bulk. Also a weaker liquid displacement conveyed by a flow annularly spreading along the substrate is visible. See also Video 2 of the Supplemental Material [48].

substrate. A spatial color plot of all fluid particles at a certain time $t$ at their respective coordinates visualizes the net displacement of the fluid in an intuitive way. We call this kind of plot a "*digital Lagrangian ink map*" or *"ink map"* for short. More details on the calculation of the Lagrangian ink map is given in the Appendix D. Clearly, the ink map representation may be considered to mimic the experimental scenario of a bubble collapsing in horizontal layers of ink confocally imaged (such an experiment would, however, be subject to many practical difficulties).

### A. Free vortex

Ink maps of the flows of the bubble that generates the free vortex (Fig. 5) are shown in Fig. 14. The distribution at the initial situation ($t = 0\,\mu$s) is given in the top left frame. Three times illustrating the successive liquid displacement are presented ($t = 425\,\mu$s, $t = 730\,\mu$s, $t = 1.85$ ms). In Fig. 15 the position of the bubble during maximum expansion is depicted. A movie of the entire ink displacement process can be found online (Supplemental Material Video 2 [48]).

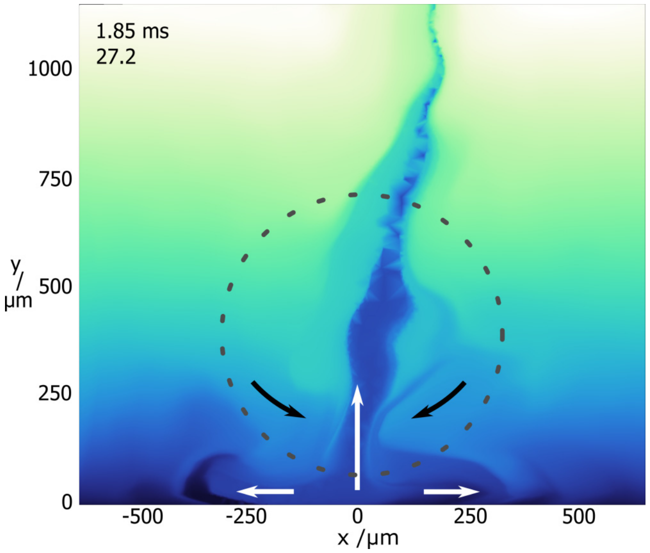

FIG. 15. Last frame of the ink displacement series of Fig. 14. Indicated is the bubble shape at maximum expansion and a sketch of the dominant directions of liquid displacement (white arrows: away and along the substrate, black toward the substrate).

From the time series, the liquid displacement by the free vortex clearly stands out and the vertical migration of the ring vortex gets apparent: The $y$-coordinate of the vortex core, $y_\mathrm{v}(t)$, representing the vortex distance to the substrate, is, for example, $y_\mathrm{v}(425\,\mu\mathrm{s}) \cong 750\,\mu\mathrm{m}$ and $y_\mathrm{v}(730\,\mu\mathrm{s}) \cong 1000\,\mu\mathrm{m}$. At $t = 1.85\,\mathrm{ms}$, the vortex has travelled already out of the imaging plane. Along with the vortex, fluid particles of the near-wall layer are incorporated into the vortical flow and get ejected into the bulk. As the free vortex travels upward, a fraction of these fluid particles are left behind, thereby the vortex "paints" a darker blue line along its trajectory. Still fluid particles from the near-wall layer may reach locations quite distant from the wall (see the small layer of blue liquid particles at $t = 730\,\mu\mathrm{s}$ around $y = 1150\,\mu\mathrm{m}$). Where the vortex passes by, it drags along fluid particles (note the greenish corona around the vortex at $t = 730\,\mu\mathrm{s}$). Besides the mixing by the free vortex, there is a pattern visible indicating a minor fluid displacement along the boundary (see the dark blue bulge at $t = 730\,\mu\mathrm{s}$ at $x \cong -250\,\mu\mathrm{m}$ and $y \cong 50\,\mu\mathrm{m}$). It results from the slower flow (this boundary layer flow has a circulation of opposite sign), pointing annularly outward over the substrate from the axis of rotational symmetry (compare to the flow field of Fig. 5 at $t \geqslant 326\,\mu\mathrm{s}$ where $0 \leqslant y \leqslant 150\,\mu\mathrm{m}$).

In Fig. 15 a schematic of the principal displacement directions is given. As where the bubble collapses liquid of the near-wall layer is displaced, in this incompressible flow subsequent streaming must replace it. The replacing liquid originates from regions located closer to the substrate; the schematic black arrows in Fig. 15 follow these flows toward the substrate, where fluid particles of greenish color are introduced into the domain of blue fluid particles.

### B. Wall vortex

The ink map of the bubble that generates the wall vortex is substantially different from the one of the free vortex. See Fig. 16 for the ink map of the bubble seeded at $\gamma = 1.67$ for four instances ($t = 550\,\mu\mathrm{s}$, $t = 1.33\,\mathrm{ms}$, $t = 3.00\,\mathrm{ms}$, and $t = 4.00\,\mathrm{ms}$, a video showing the entire displacement process can be found in Video 2 of the Supplemental Material [48]). In the first frame, the bubble shape during maximum expansion is depicted (it is reached at $t = 30\,\mu\mathrm{s}$). Already in the earliest ink map ($t = 550\,\mu\mathrm{s}$) the fluid displacement by the two substantial underlying flows can be perceived. In the center, with the jet and subsequent flows, yellow to white coded fluid particles arrive at the

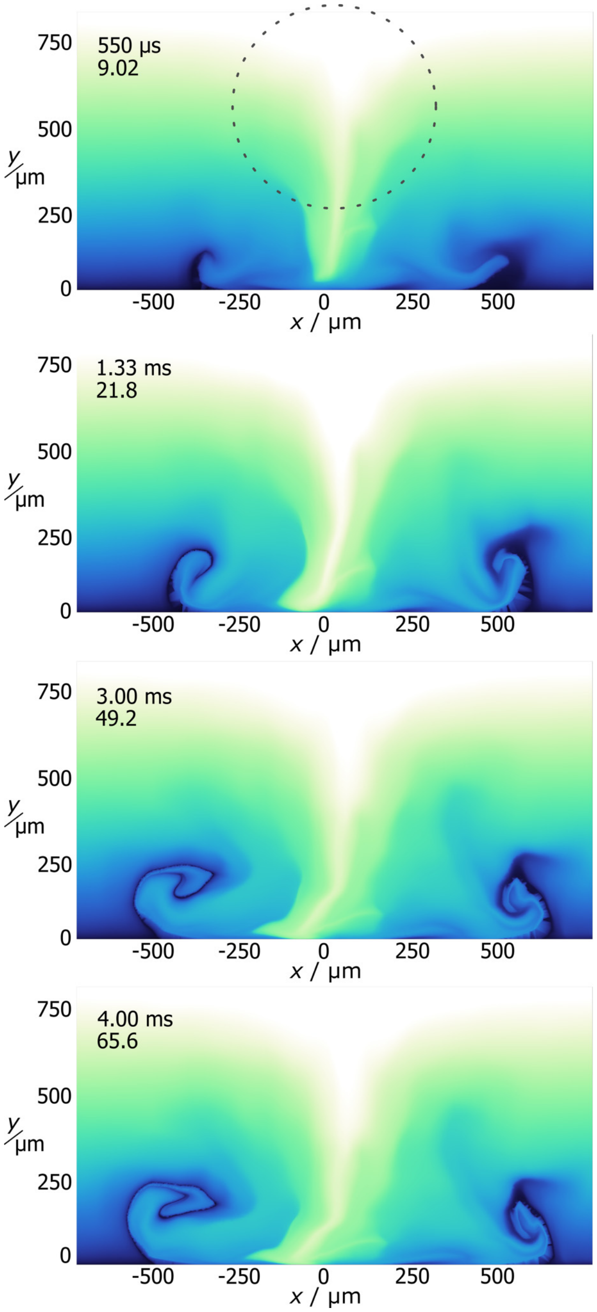

FIG. 16. Vertical ink map for the bubble of Fig. 8 ($\gamma = 1.67$) generating a wall vortex. The boundary is located horizontally at $y = 0$. Absolute times $t$ and nondimensionalized times $\tau$ are given in each frame. Two main streams are responsible for the net displacement and mixing: (1) Along with the jet, fluid is pushed from the bulk toward the boundary (white-yellowish, vertical tip). (2) Along with the radially spreading vortex ring, fluid is pushed horizontally outward (from the symmetry axis) over the substrate. Thereby, the boundary layer lifts off and winds up with the vortical flow (dark blue "spiral"). Times respective to bubble seeding are given in each frame. Initial situation at $t = 0$: horizontal, colored layers from white-yellow (top) to dark blue (bottom) as in Fig. 14.

substrate. As liquid is dragged from the top to the bottom (the white liquid protrudes downward), liquid is also pushed horizontally out of the image plane. With the ring vortex that is generated around the south pole of the maximally expanded bubble, green coded fluid particles (originating about $150\,\mu$m to $250\,\mu$m distant from the axis of rotational symmetry, around where the vortex inner core is generated) circulate along the substrate and wrap up dark blue fluid particles from the boundary layer. The subsequent ink maps essentially illustrate the further mixing and fluid displacement by the wall vortex that stretches radially along the substrate. Thereby the boundary layer is further wrapped up and lifted about $200\,\mu$m off the substrate. It is noteworthy that the ink associated with the vortex extends radially for more than $500\,\mu$m over the substrate, whereas the maximum bubble radius is only $310\,\mu$m. Evidently, as the vortex wraps up the dark blue boundary layer, it significantly increases the interfacial area (here, in 2D projection the interfacial length) and thus the local color gradients. Hereof follows the interest in the vortex for the acceleration of mass transfer limited processes. Additionally, the up wrapping of the boundary layer, bulk liquid is fed toward the substrate surface. It can also be observed from the ink maps that the fluid elements entrained in the vortex are not the same that form the axial jet. Instead, the fluid elements that impact on the substrate with the vortex originate from locations around $y = 300\,\mu$m, $|x| \geqslant 250\,\mu$m—the jet tip in comparison, spans only about $|x| < 50\,\mu$m.

Bubbles generated at standoffs larger than the considered $\gamma = 1.67$ produce flow patterns that are qualitatively the same. Only the initial vortex diameter at generation decreases and the maximum radial extension of the vortex over the substrate strictly decreases (see Refs. [29,42]).

## VI. SUMMARY AND DISCUSSION

A bubble collapsing in the vicinity of a solid substrate generates complex fields of strong flows important for many applications of cavitation. These flow fields together with the time-resolved details of their generation were investigated experimentally on a single-bubble level. To that end, single bubbles (maximum radius around $400\,\mu$m) were seeded by a laser at confined distances from a solid substrate and long-term image series of the bubble-shape dynamics were recorded synchronously from two perspectives. The corresponding unsteady flow fields were measured synchronously with the shape dynamics by a high-speed $\mu$PIV/PTV technique. From the flow fields, the total liquid displacement actuated by a single bubble was calculated and visualized in digital Lagrangian ink maps.

Among several flow phenomena associated with the bubble collapse, especially the ring vortex generated by the collapsing bubble was analyzed. It can exhibit significant shear rates on the substrate and largely determines the liquid displacement. Bubbles can generate two different types of ring vortices: a free vortex or a wall vortex. They differ by the sign of circulation and consequently have a different translation direction so that either liquid is ejected from the near-wall boundary layer or pushed along the substrate. The two flow patterns can be grasped at a glance in Figs. 14 and 16. Both vortex types are generated with similar magnitudes of circulation, but the wall vortex is more damped while the free vortex travels far away from the boundary into the liquid bulk.

During its dynamics, an initially spherical bubble can take a toroidal shape. The toroidal bubble is subject to severe deformation by the surrounding flow field and the vortex formation is a result of the interplay between the flow field and the torus bubble dynamics. An intriguing situation is presented in Fig. 7 at $\tau = 1.36$. Even though the gas phase is around maximum expansion, the bubble is surrounded by an intense and complex flow field, for instance, the bubble torus still expands outward, while it already collapses from the inner side. Isolated cases of shrinking and instable fluid tori were investigated by Pairam and Fernández-Nieves [67] and Darbois Texier *et al.* [68]. Darbois Texier could derive a Rayleigh-Plesset-like differential equation describing the shrinking of a liquid torus. Still, it cannot describe our case, because it models torus shrinking driven by surface tension and minimization of free energy. In contrast here, energy is mainly stored in the flow field (besides the compression of the gas phase). Thus, in our case, both the Weber number and the Reynolds number are much larger because torus interface velocities are a thousand to a million times faster than in the aforementioned works. Here, to understand the toroidal bubble dynamics, knowledge of the flow fields generated during bubble collapse is required.

A general peculiarity of bubbles collapsing in the vicinity of boundaries is the sensitivity for the emergence of certain aspects of the bubble and flow dynamics toward the standoff distance. In particular, it is shown here that the direction of vortex circulation depends critically on the standoff distance $\gamma$. For $0.5 \leqslant \gamma \leqslant 1.30$, a free vortex is generated. This is a vortex that migrates perpendicularly away from the substrate. It is formed by annular flows rushing inward along the boundary, toward the axis of symmetry. They are substantially driven during the (toroidal) collapse of the flattened bubble, i.e., here during the second collapse before which the bubble takes a flattened shape along the substrate. Then the collapse from the outer torus walls inward dominates over the collapse from the inner torus outward so that the downward directed axial jet stagnates. So, the initially annular jet proceeds as an axial one upward along the axis of symmetry, perpendicularly away from the boundary. For the microsized bubbles under consideration, the first emergence of significant circulation that will form the free vortex is found about 100 $\mu$s ($\sim$1.4 $T_{\mathrm{L}}$) after the bubble generation and a further development into a stable ring vortex with an approximately Gaussian-distributed vorticity is completed after about 200 $\mu$s ($\sim$2.8 $T_{\mathrm{L}}$, with $R_{\max}$ being in the order of 400 $\mu$m). Once formed, the free vortex translates solely driven by self-propulsion.

On the other hand, a bubble collapsing in the vicinity of a solid boundary at a larger standoff distance ($\gamma \geqslant 1.36$) generates a wall vortex: a ring vortex that migrates toward the wall and radially stretches over the substrate. By the time resolved measurement of the flow field together with the bubble shape dynamics, we can provide an experimental perspective on its formation. It is well known that generally a jet can generate a ring vortex. This is widely exploited in vortex generators, such as vortex cannons, where by sudden acceleration of fluid in a confined typically tubelike geometry a ring vortex is produced when the jet leaves a (submerged) nozzle. The ring is produced as the boundary conditions abruptly change, typically from a no-slip condition at the generator wall to a slip condition after passing the nozzle (for an overview, see Ref. [69]). Probably the quite widespread application of this type of ring vortex generators is the reason why the idea remains that this mechanism holds as well for the bubble generated ring vortex as the axial jet impinges through the opposite wall [70]. However, this picture is incomplete, and the vortex ring is not formed at the location where the jet pierces through the opposite bubble wall but around the ring of the toroidally collapsed bubble. In fact, one has to consider that while a vortex generator has a static orifice (with no slip boundary condition) here the vortex generation is determined by the motion of the bubble boundary. In the final stage of the toroidal bubble collapse, in addition to the axial jet, there is an annular flow following the collapsing torus from its outer side. Both flows are initially separated by the gas domain that exhibits a free-boundary condition and therefore allows extremely high velocity gradients to form between them. Finally, a circular flow around the toroidally collapsing and virtually vanishing gas phase is generated. Consequently, the vortex ring is formed in such a manner that its core is located in the ring into which the toroidal bubble collapses, not where the jet protrudes through the bubble. Thus, we can identify a collapsing bubble as a very efficient and unique ring vortex generator. Furthermore, we can greatly justify experimentally the numerical technique introduced by Wang *et al.* [71] who seeded a vortex ring inside a torus bubble in order to calculate its dynamics (this technique was also used by Lee *et al.* [72], Wang [73], and Zhang *et al.* [74]).

Within the wall vortex, along a significantly large substrate surface, notable wall shear forces are exerted predominantly by the ring vortex. The radius of the (circular) region of high wall shear from the stretching vortex can exceed the maximum radius of the vortex-generating bubble, and in this way, a bubble seeded at a larger standoff distance can produce a flow that spans over a larger substrate surface than one that is generated closer. The reason is that the vortex entrains quite some liquid and most of the kinetic energy is expected to be bound to the vortex motion (see also Ref. [75]); the prominent and violent axial jet is a phenomenon of energy concentration but the jet impacts on the substrate only in a small area around the axis of symmetry. In addition, significant annular flows directed inward, opposite to the jet and thereby inhibiting it, are generated, mainly during the second collapse (for around $\gamma = 1.4$). For standoffs larger than the ones presented here,

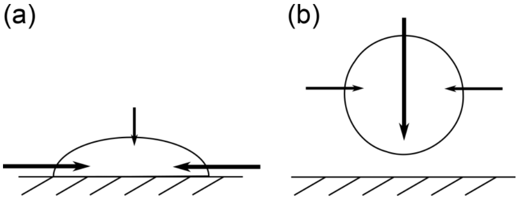

FIG. 17. Simplified sketch of the flows generated during the second bubble collapse that are involved in the production of either a free or a wall vortex. (a) Free vortex: The flat, elongated bubble collapses mainly from the outer torus, high pressures occur at the center and the axial jet quickly stagnates. (b) Wall vortex: The axial jet pierces through the bubble and impacts on the substrate before the gas phase.

the dynamics stay qualitatively the same (see Ref. [42] for a standoff-dependent quantization of the substrate interaction of the bubble induced wall vortex by the time dependent mass transfer enhancement toward the substrate).

For initially "perfectly" spherical bubbles, the two regimes are divided by a very sharp transition at $1.30 < \gamma < 1.36$. In this standoff range, no ring vortex is observed, instead the liquid comes to rest quickly when the bubble disintegrates. The reason that no ring vortex is produced seems to lie in the toroidal bubble collapse that proceeds equally from the inner and the outer torus so that the respective flows following the collapsing bubble walls then just collide. In this situation, more energy is dissipated into shock wave emission. Indeed, Vogel *et al.* [25] experimentally found indications for a maximum of shock wave emission during the second collapse for a standoff between $\gamma = 1.25$ and $\gamma = 1.45$. This is a regime that should possibly be avoided to protect sensitive surfaces from erosion (compare also Refs. [29,37]). It should be considered, however, that the exact $\gamma$-value of transition may also depend on further parameters. In particular, for much larger bubbles buoyancy may play a role, while the dynamics of much smaller bubbles may be dominated by forces from surface tension or viscosity. Simulations might confirm and explore this transition if they are capable of a reliable modelling of the repeated topology changes of the gas phase.

The reasons for the generation of either of the oppositely directed vortices lie deep in the dynamics details of bubble collapse and involved flows. The key frames showing the differences between the generation of the oppositely directed vortices are Fig. 3, $\tau = 1.07$; Fig. 7, $\tau = 1.36$, 1.75, and Fig. 9, $\tau = 1.44$, 1.80, respectively. A very simplified sketch of the flows involved in the vortex formation is given in Fig. 17. In the case of the more distant bubble (producing the wall vortex) the axial jet of the first collapse spreads over the substrate mainly before the gas phase touches (and rebounds) on the substrate; compare the shape dynamics in Fig. 3 at $\tau = 1.07$. The gas shape follows the direction of the jet toward the substrate and collapses predominantly from the north pole [see Fig. 17(b)]. Thereby, the ring vortex moving toward the substrate is generated. In contrary, in the case of the free vortex, the jet and gas phase reach and spread over the substrate at about the same time (see, for example, Fig. 3 at $\tau = 1.07$). In that situation, the bubble rebounds in a flat shape on the substrate and all flows directed toward the substrate, away from the substrate or along the substrate are generated at about the same distance from the wall (see Fig. 7, $\tau = 1.36$), thus generating mainly an annular jet. The flat-shaped bubble then collapses predominantly from the outer torus. This way only a weak axial jet that quickly comes to stagnation forms while the liquid from the annular jet is ejected finally upward into the bulk.

From the time-integration of the full, unsteady flow fields the net fluid displacement by collapsing bubbles was calculated and presented in digital Lagrangian ink maps. Thereby detailed insight is gained into the mass transfer enhancement and mixing potential from transient cavitation bubbles on a single bubble level. It is evident that repeated, solely radial oscillations cannot contribute to mixing as they do not create a net fluid displacement; indeed, tracer particles are found at their initial positions after some radial bubble oscillations. Instead, in order to achieve any mixing, the symmetry has to be broken, here by the solid boundary so that via a pressure gradient a Kelvin impulse is generated. The oscillating bubble (its centroid) translates through the liquid—it may be considered as a dipole—generating some circulation. Consequently, the total liquid displacement is largely constituted by the vortex ring formed during bubble dynamics. It carries most of the momentum in the flow and persists for a quite long time. In general, ring vortices can achieve an efficient mixing engulfment and straining of interfaces between species or liquid layers (see, for example, Ref. [76]). These effects are well perceived in the Lagrangian ink maps. With the free vortex, fluid from the near-wall layer is entrained and ejected far into the bulk. With the wall vortex, a jetlike pattern of liquid is pulled toward the substrate along the axis of symmetry and the near-wall liquid layer is pushed radially outward, whereby it is wrapped up into spirallike structures. Thus, even though free and wall vortex dispose of about the same absolute amount of circulation and are produced by bubbles that first seem to develop very similar collapse dynamics, they are responsible for quite different mixing patterns. In comparison, the effect on the net liquid displacement by the prominent substrate-perpendicular jet that develops during the aspherical bubble collapse is minor. Its volume flux is less and its duration is shorter due to repeated reversal of the flow direction (see, for an estimation of the jet volume, Ref. [77], and for an approximate standoff-dependent jet-scaling, Ref. [78]).

In addition to the flow-field analysis, time series of shape dynamics were presented. In contrast to previous works, here one and the same bubble was long-term imaged, synchronized from two (perpendicular) perspectives. The ring vortex is also visible in the shape dynamics due remnant bubbles (e.g., gas phase entities that are split from the bubble after repeated collapses) that translate together with the ring. The major difference observed in the shape dynamics with respect to the type of generated vortex lies in the radius of the collapsing torus bubble at the second collapse. This radius can be considered an indicator for the timing and intensity of the axial jet compared to the annular one.

## VII. CONCLUSIONS

Hydrodynamic and acoustic cavitation gained their significance in technical applications to a large extent from hydrodynamic effects induced by collapsing cavitation bubbles. The produced flow fields are highly unsteady and often possess impressive shear. Therefore, experiments are demanding, and consequently so far experimental data of bubble-induced flow fields are scarce. Thus, despite many advances already made in the field, the physics of flow generation of aspherically collapsing bubbles are by far not fully understood yet. In this context, we provide detailed insight into the unsteady flows generated during the aspherical collapse of single microsized bubbles in the vicinity of a solid boundary. Our experimental data may also close a gap for the comparison to numerical simulations as it offers (1) long-term observations of the gas-shape dynamics of one and the same bubble from two perpendicular perspectives synchronously, and (2) detailed long-term measurements of the flow field in conjunction to synchronous gas shape imaging. The flow field was obtained by a hybrid PIV/PTV technique that was implemented at the current technical limits in terms of temporal and spatial resolution being capable of resolving many hydrodynamic details of bubble collapse and subsequent phenomena.

It is demonstrated that resembling bubbles can produce very different flow patterns, crucially depending on the standoff distance of the bubble to the substrate. In particular, there are two different types of ring vortices that are generated by the collapsing bubble: either a free vortex, a ring vortex that translates into the bulk, away from the solid boundary; or a wall vortex, a ring vortex of opposite circulation that hence moves toward the solid boundary and subsequently spreads radially over the substrate. The ring vortex determines a large part of fluid motion and therefore methods for its controlled application are desired. For example, the free vortex is capable of ejecting a large portion of wall-near liquid into the bulk, which may be used in emulsification, mixing applications or in order to increase the mass transfer from (reactive) surfaces.

The wall vortex type may find applications in surface cleaning as it exhibits a significant shear flow along a larger region on the substrate. In biophysical or medical contexts—where ultrasound has already shown to improve drugs or genes delivery into cells—the vortex may play a significant role to permeabilize vesicles or cell membranes by shearing the membrane without disrupting it. However, cell membranes constitute flexible boundaries in contrast to the rigid ones under investigation here. In general, a transfer of our results to other situations where jetting bubble collapses occurs is desirable, in particular, to cases of bubbles collapsing close to soft instead of rigid boundaries, bubbles in pressure gradients of flow fields or acoustic fields, or relative motion of bubble and liquid. The prediction of the vortical flows in these cases can be difficult as it may be quite sensitive to the exact geometry. Here, further experimental clarification is needed. Still, the generation of strong and longer living vortices in connection with jetting is to be expected. Thus, in various contexts, such as mixing or emulsification of liquids with acoustic or hydrodynamic cavitation, the contribution for the process from the vortex is possibly higher than that from the jet itself.

Finally, we introduce a powerful tool that we call *Lagrangian ink mapping*. It is a representation technique for understanding the structure of unsteady flow fields and the fluid displacement therein. Lagrangian ink maps make the huge datasets that represent unsteady flow fields, which are often encountered in complex experimental scenarios (such as collapsing bubbles), easily accessible. This is achieved by a data reduction from time integration of the flow field together with an intuitive color coding. Thereby, it was even possible to visualize the winding up of boundary layers and fluid lamellae. This in turn can be considered a confirmation of the accuracy of the PIV/PTV method employed. Thus, our results show that Lagrangian ink maps can facilitate the analysis of situations with unsteady flow fields and have the potential to become a standard representation technique.

## ACKNOWLEDGMENTS

We are particularly indebted to Prof. W. Lauterborn for valuable feedback and thank all group members of the Christian Doppler Laboratory for Cavitation and Micro-Erosion at the Drittes Physikalisches Institut for support and stimulating discussions. We thank for support by Lam Research AG, Austria, especially F. Holsteyns (now at IMEC Leuven, Belgium) and A. Lippert (now at Osram Opto Semiconductors). F.R. and R.M. gratefully acknowledge the financial support by the Austrian Federal Ministry of Economy, Family and Youth and the Austrian National Foundation for Research, Technology and Development. S.R.G.-A. and C.-D.O. acknowledge financial support from the Office of Naval Research under Grant No. N62909-16-1-2139.

## APPENDIX A: EXPERIMENTAL DETAILS

In this section, more details on the employed devices are given and some experimental difficulties that originate from the specific flow characteristics and that had to be overcome are discussed.

The shear rates generated by a collapsing bubble are high, the flow is unsteady, even transient, illumination conditions change due to scattering at the rapidly deforming gas phase (actually, a three-phase moving boundary is imaged), and the flow velocities exhibit a high dynamic range spanning over different time scales. Those flow properties often pose contradictious requirements on the measurement technique.

Fast flows (and consequently short exposure times, here down to $7.5\,\mu$s) demand for bright luminous, i.e., large particles. The fluorescent particles are volumetrically dyed and their light emission is proportional to the third power of the particle radius. At the same time however, transient flows demand for agile, which means small particles that instantaneously follow the flow and are not affected by the high shear rates. For the employed equipment and bubbles under investigation, an optimum for the particle diameter of about $5\,\mu$m has been experimentally determined. The particle response time is $1.46\,\mu$s, according to the formula given by Wereley and Meinhart [79] and therefore sufficient to follow most of the bubble induced flows. Only to the jet tip some limitations apply, its resolution by a particle velocimetry technique is prohibited due to its small-scale, high shear rates, and fast acceleration, so that conditions for particles ideally following the fluid are not given.

The high shear rates (the small-scale flow field) and the flow field data retrieval on only one and the same bubble over the whole time span require high particle seeding densities which in turn are limited by the requirement of a sufficiently undisturbed optical accessibility in order to image the bubble shape and to optically deliver the respective laser energy for the bubble generation. This is aggravated as a certain distance from the bubble center to any wall other than the test boundary at the top cover of the cuvette has to be provided in order to leave the bubble dynamics unaffected from such additional boundaries (a minimum distance of about 10 $R_{\max}$ can be considered to be sufficient). Hence, a long-distance microscope objective that is not in contact with the liquid is employed for laser focusing (Olympus, U Plan FL N, 10X, NA = 0.3, working distance 10 mm), see also Fig. 1. For a high numerical aperture, the laser beam is first expanded before focusing (plano-concave lens BK7, $-f = 50$ mm, collimated by a plano-convex lens). The inner dimensions of the cuvette are designed in such a manner that distances of the bubble to further walls are sufficiently large (10 $R_{\max}$) but at the same time kept as short as possible to minimize the optical path length through the liquid to avoid light scattering at the tracer particles. To counteract settlement and coagulation of the tracer particles, the test section is equipped with an inlet-outlet port for repeated mixing in between the experiments to assure a homogenous particle distribution when the experiment starts. Furthermore, the use of glass walls, instead of plastics, reduces the tendency of the particles to adhere to the cuvette walls. The particles are excited by the beam of a CW laser. It is shaped into a thin light sheet (width about 140 $\mu$m at beam waist) and coupled into the cuvette through the bottom window. The light-sheet optics (plano-concave cylindrical lens: Edmund Scientific, NT68-056, $-f = 50$ mm; achromatic doublet lens Thorlabs, AC254-060-A1, $f = 60$ mm; dielectric mirror: Thorlabs, CM1-E02) are mounted on a precision rail and attached to a three-axis stage in order to accurately position the laser sheet in the test section to slice the bubbles through its center and meet the solid boundary perpendicularly (see the inset in Fig. 1 for an example image). Due to the good optics, the width of the light sheet is not limited by the optics itself but is rather determined by the broadening of the light sheet due to scattering at the tracer particles.

The necessity for a high particle seeding density together with long optical path lengths give raise to image noise from scattering at the tracer particles. As to counteract the scattering noise, besides certain measures in data evaluation (see Appendix B), with adequate lasers and optical filters, the optical spectrum is split as for the experimental subsystems to not interfere: the blue spectral component is used for bubble imaging, the red for tracer particle imaging, and the green for tracer excitation and bubble seeding. Therefore, the PIV camera is used with a low pass filter blocking the green and blue spectral part of the light (filter: MidOpt LP550) to detect only the red spectrum from the fluorescent tracer particles that have their peak emission wavelength around 617 nm. The bubble shape is imaged in transmission light (metal halide lamp, type: LS-M250, Sumita, Japan, used together with a light guide and collimating optics and bandpass filters) using only the blue spectral component by optical bandpass filters, thereby avoiding spurious excitation and scattering on the tracer particles.

Additionally, to prevent the cameras from damage by the intense laser light, for both cameras a notch filter is placed in front of the CCD (filter: Semrock, NF20-532S-25). Furthermore, both cameras are connected to a three-axis translation stage for adjustment of the imaging section. The timing of the measurement procedure (triggering of the laser flash and Q-switch as well as the camera exposures) is controlled with a pulse generator (BNC, model 575). A time series of sample particle images can be found in the Supplemental Material (Fig. 1).

## APPENDIX B: EVALUATION OF $\mu$PIV/PTV DATA

To cope with demanding conditions of high shear rates and velocities (locally producing particle image streaks) at solid boundaries, it proved to yield best results to employ a manual PTV approach that is combined with an adapted PIV evaluation. Thus, local velocities from PIV and PTV are obtained separately and combined by binning. Here the PIV evaluation is based on the calculation of the mean square difference between two subsequent particle images (= images from the PIV camera) instead of the cross-correlation which is realized in conventional algorithms for PIV evaluation. The exact procedure is described below. For all data evaluation, scripts in Matlab are developed.

As with conventional PIV evaluation techniques, the flow velocity during one sample interval $\Delta T_{\mathrm{PIV}}$ is derived from the particle displacement between two subsequently taken particle images, recorded by the PIV camera at times $t_1$ and $t_2 = t_1 + \Delta T_{\mathrm{PIV}}$. To do so, the entire particle image at time $t_1$ is partitioned into smaller windows $W_{t_1}$ (interrogation areas) each of size $X_{t_1} \times Y_{t_1}$, permitting some overlap between them. The subsequent particle image, taken at time $t_2$, is partitioned into the same number of windows with the same center coordinates as before, but now each window $W_{t_2}$ is of larger size $X_{t_2} \times Y_{t_2}$, thus $X_{t_2} > X_{t_1}$ and $Y_{t_2} > Y_{t_1}$. Now, in analogy to the correlation space, we define the *rms space* for a pair of windows $W_{t_1}$ and $W_{t_2}$ having the same center coordinates. It is calculated as the square-root of the sum of the pixel-wise squared difference of grey values between $W_{t_1}$ and $W_{t_2}$ for all possible $[(X_{W_{t2}} - X_{W_{t1}})\,(Y_{W_{t2}} - Y_{W_{t1}}) + 1]$ image shifts between $W_{t_1}$ and $W_{t_2}$. The displacement coordinates of the minimum in the rms plane give the fluid displacement for each window pair. For subpixel accuracy, a second order polynomial fit is performed in the rms space around the minimum.

Unlike cross-correlation techniques that are often implemented to work on windows of the same size, the rms technique easily allows, and actually requires, PIV windows of different dimensions, giving an advantage for the resolution of the near-wall flows. Furthermore, it is especially suited for low particle seeding densities (and high velocities) due to significantly increased robustness against particles leaving a window within $\Delta T_{\mathrm{PIV}}$, as the window $W_{t_2}$ is larger than $W_{t_1}$ so that $W_{t_2}$ will usually contain the respective particle. Out-of-plane motion is not critical here as it occurs predominantly gradually.

Accuracy of the method is proved for artificial test images of Gaussian peaks (a particle actually has the image of an Airy-disk on the camera CCD, however, at the present optical scales it can be modelled as Gaussian) and we obtain an error in the determination of the displacement only in the per mil range. We estimate the error of the so determined velocity to be 0.25 pixel per frame, that corresponds to $1.15\,\mu\mathrm{m}/\Delta T_{\mathrm{PIV}} = 0.02\,\mathrm{ms}^{-1}$ to $0.16\,\mathrm{ms}^{-1}$, depending on the frame rate. This is less than 1% of the maximum velocities. Thus, the error in localizing the centroid of the tracer particles is not critical.

As flow velocities span over several scales of magnitude, the PIV time step of the evaluation is adaptive. For evaluation windows where the flow velocity is significantly lower than 1 pixel per frame, the PIV time step is increased to multiples of the PIV frame time $T_{\mathrm{PIV}}$.

Prior to PIV-data evaluation, images are digitally improved to reduce (pixel) noise, camera striping and nonuniform (background) illumination: a CLAHE-filter (contrast limited adaptive histogram equalization), spatial low-pass filter and high-pass filters are applied. The filter slope is modelled as a three-term cosine function, designed to have rapidly decaying higher order sidelobes to avoid artefacts and avoid bleeding of the particle brightness into neighbouring evaluation windows.

For the joint representation of the flow field and the bubble, the images of the bubble camera are overlaid to the flow field, after adequate scaling and rotation. Data points are masked if more than 25% of a window $W_{t_1}$ are located within the gas phase of the bubble.

For high velocities, e.g., when the velocity $v$ is larger than $1\,\mathrm{pixel}/T^{\mathrm{e}}_{\mathrm{PIV}}$, particle streaks occur, and for high shear rates, e.g., when the velocity significantly changes within one window, the PIV technique is likely to produce erroneous data. Thus, for particles located in PIV windows meeting the aforementioned criteria, a manual PTV technique is applied. A special program to ease the manual tracking process has been developed for this purpose. It allows to track particles on an arbitrary grid. For subpixel accuracy of the PTV data, the image is digitally up-sampled and the same subpixel estimator as from the PIV evaluation is applied, this time in coordinate space of the particle image.

With this technique and the applied exposure times here, it is possible to track particles with velocities up to about $20\,\mathrm{ms}^{-1}$, where we estimate the error to be about 7%.

## APPENDIX C: DETERMINATION OF QUANTITIES DERIVED FROM THE FLOW FIELD

The flow fields depicted here, for a compact representation, are plotted with a reduced spatial resolution. For derived quantities such as shear rates, total kinetic energy, total momentum, or the vorticity, a finer resolution is employed.

For the derivation of global quantities such as the total kinetic energy and the total momentum, rotational symmetry of the flow field is assumed. The location of the axis of symmetry is determined separately for each row of PIV evaluation windows as the centroid of the velocity $v_x$ (the velocity component perpendicular to the axis of symmetry).

The circulation $\Gamma$ of the liquid, important here to characterize the ring vortex, in general can be derived from the line integral over the vorticity $\omega$ around a simply connected surface S: $\Gamma = \int \omega \, dS$ (compare the white sketch in the vorticity plot of Fig. 10).

However, here the determination of vorticity is experimentally demanding: The vorticity is concentrated to a small core and it is derived from experimental data by two successive derivatives (a temporal one for the velocity and subsequent spatial for the vorticity) introducing quite some noise. Additional concerns result from the sampling of a convective, circular flow on a rectangular grid. To still achieve robust results, the circulation is derived in the following way: First the spatial resolution of the vorticity is digitally increased, using cubic 2D interpolation, to account for the velocity sampling on a rectangular grid. Let $a$ denote a radial coordinate, the distance to the vortex core center (see Fig. 10) and assume locally a rotational symmetry in the measurement plane around the vortex core, then the vorticity profile $\omega(a)$ is fitted with a Gaussian $\omega(a) = K \exp\left(\frac{a}{\sigma}\right)^2$, where $K$ and $\sigma$ are the fit parameters. The circulation of the velocity field in the $x/y$ plane is then given by: $\Gamma = \int_0^\infty 2\pi r K \exp\left(\frac{a}{\sigma}\right)^2 dr = \pi K \sigma^2$. For the fit $\omega(a)$, data points at a maximum distance of $a_{\max} = \frac{1}{2} D_v$, or where the vorticity changes sign, whatever occurs at smaller distances, are considered. From the Gaussians at subsequent times, the temporal evolution of the circulation of the velocity field in the $x/y$ plane is determined by: $\Gamma = \int_0^\infty 2\pi r K \exp\left(\frac{a}{\sigma}\right)^2 dr = \pi K \sigma^2$. Note that a determination of the circulation by the path integral $\Gamma_C = \oint_C \vec{v} \, d\vec{l}$ (see also sketch in Fig. 10, left) yields consistent results (deviation smaller than 10%) but contains more noise.

## APPENDIX D: CALCULATION OF LAGRANGIAN INK MAPS

To calculate the ink maps, paths of individual fluid particles are tracked. To do so we proceed in the following way: The spatial resolution of the full-field PIV/PTV data is digitally increased tenfold (per dimension) by linear interpolation so that the spatial coordinates of the velocity vectors lie so close together that each coordinate can indeed be considered to describe the location of one "fluid particle." In addition, the temporal resolution is digitally increased by a factor of fifteen by interpolation. Then the trajectories of all fluid particles are calculated by iterative evaluation of the convection equation $\vec{x}_n(t + \Delta T_{\text{mix}}) = \vec{x}_n(t) + \vec{v}_n \Delta T_{\text{mix}}$, where $\vec{x}_n$ is the coordinate of the $n$th fluid particle, $\vec{v}_n$ its velocity, and $\Delta T_{\text{mix}} = \frac{1}{15} \Delta T_{\text{PIV}}$ the time step taken for the calculation. In order to assure that fluid particles do not migrate through the substrate by numerical errors, the velocity dataset is zero-padded at the location of the substrate ($y = 0$), similar to the constraint imposed by a no-slip boundary condition. Initially, each fluid particle is "ink-labeled," i.e., to each fluid particle, a color according to its $y$-coordinate at $t = 0$ is assigned: here we use dark blue for fluid particles starting at the substrate, and lighter green to white colors for fluid particles starting at locations more remote from the substrate. The assigned color of one fluid particle is never changed and can be considered a fluid-particle label. Thereby, it is assured that one fluid particle represents an indivisible "particle," e.g., it is immiscible and in particular does not experience diffusion.

A spatial plot of all fluid particles at a certain time $t$ at their respective coordinates $\vec{x}_n(t)$ with their initially distributed color visualizes the net displacement of the fluid in an intuitive way. We call this kind of plot a "*vertical digital Lagrangian ink map*" or *"ink map"* for short. The described initial inking of fluid particles according to their $y$-coordinate and consequent color gradient of the domain along the vertical axis allows for the visualization of mixing in vertical direction. The same procedure but with inking according to the respective $x$ coordinates instead would as well allow for the visualization of mixing in the horizontal direction and where the corresponding representation gives a "*horizontal ink map.*"

[1] T. G. Leighton, *The Acoustic Bubble* (Academic Press, San Diego, 1994).

[2] C. E. Brennen, *Cavitation and Bubble Dynamics* (Oxford University Press, Oxford, 1995).

[3] W. Lauterborn and T. Kurz, Physics of bubble oscillations, Rep. Prog. Phys. **73**, 106501 (2010).

[4] W. Lauterborn, Numerical investigation of nonlinear oscillations of gas bubbles in liquids, J. Acoust. Soc. Am. **59**, 283 (1976).

[5] F. Reuter, S. Lauterborn, R. Mettin, and W. Lauterborn, Membrane cleaning with ultrasonically driven bubbles, Ultrason. Sonochem. **37**, 542 (2017).

[6] R. Dijkink, S. Le Gac, E. Nijhuis, A. van den Berg, I. Vermes, A. Poot *et al.*, Controlled cavitation—cell interaction: Trans-membrane transport and viability studies, Phys. Med. Biol. **53**, 375 (2006).

[7] M. Postema, *Fundamentals of Medical Ultrasonics* (CRC Press, Boca Raton, 2011).

[8] C. E. Brennen, Cavitation in medicine, Interface Focus. **5**, 20150022 (2015).

[9] C. F. Naudé and A. T. Ellis, On the mechanism of cavitation damage by nonhemispherical cavities collapsing in contact with a solid boundary, J. Basic Eng. **83**, 648 (1961).

[10] N. D. Shutler and R. B. Mesler, A photographic study of the dynamics and damage capabilities of bubbles collapsing near solid boundaries, J. Basic Eng. **87**, 511 (1965).

[11] A. Shima, K. Takayama, Y. Tomita, and N. Ohsawa, Mechanism of impact pressure generation from spark-generated bubble collapse near a wall, AIAA J. **21**, 55 (1983).

[12] W. Lauterborn, Kavitation durch Laserlicht (Cavitation by laser light), Acustica **31**, 51 (1974).

[13] W. Lauterborn and H. Bolle, Experimental investigations of cavitation-bubble collapse in the neighbourhood of a solid boundary, J. Fluid Mech. **72**, 391 (1975).

[14] O. Lindau and W. Lauterborn, Cinematographic observation of the collapse and rebound of a laser-produced cavitation bubble near a wall, J. Fluid Mech. **479**, 327 (2003).

[15] M. S. Plesset and R. B. Chapman, Collapse of an initially spherical vapor cavity in the neighborhood of a solid boundary, J. Fluid Mech. **47**, 283 (1971).

[16] J. R. Blake, B. B. Taib, and G. Doherty, Transient cavities near boundaries. Part 1. Rigid boundary, J. Fluid Mech. **170**, 479 (1986).

[17] A. Pearson, J. R. Blake, and S. R. Otto, Jets in bubbles, J. Eng. Math. **48**, 391 (2004).

[18] M. Kornfeld and L. Suvorov, On the destructive action of cavitation, J. Appl. Phys. **15**, 495 (1944).

[19] T. B. Benjamin and A. T. Ellis, The collapse of cavitation bubbles and the pressures thereby produced against solid boundaries, Philos. Trans. R. Soc. A Math. Phys. Eng. Sci. **260**, 221 (1966).

[20] T. S. Lundgren and N. N. Mansour, Vortex ring bubbles, J. Fluid Mech. **224**, 177 (1991).

[21] J. P. Best, The formation of toroidal bubbles upon the collapse of transient cavities, J. Fluid Mech. **251**, 79 (1993).

[22] Q. X. Wang, K. S. Yeo, B. C. Khoo, and K. Y. Lam, Vortex ring modelling of toroidal bubbles, Theor. Comput. Fluid Dyn. **19**, 303 (2005).

[23] R. P. Tong, W. P. Schiffers, S. J. Shaw, J. R. Blake, and D. C. Emmony, The role of "splashing" in the collapse of a laser-generated cavity near a rigid boundary, J. Fluid Mech. **380**, 339 (1999).

[24] E. A. Brujan, G. S. Keen, A. Vogel, and J. R. Blake, The final stage of the collapse of a cavitation bubble close to a rigid boundary, Phys. Fluids. **14**, 85 (2002).

[25] A. Vogel and W. Lauterborn, Acoustic transient generation by laser-produced cavitation bubbles near solid boundaries, J. Acoust. Soc. Am. **84**, 719 (1988).

[26] W. Lauterborn and A. Vogel, Shock wave emission by laser generated bubbles, in *Bubble Dynamics and Shock Waves* (Springer, Berlin, 2013), pp. 67–103.

[27] Y. Tomita and A. Shima, Mechanisms of impulsive pressure generation and damage pit formation by bubble collapse, J. Fluid Mech. **169**, 535 (1986).

[28] A. Vogel, W. Lauterborn, and R. Timm, Optical and acoustic investigations of the dynamics of laser-produced cavitation bubbles near a solid boundary, J. Fluid Mech. **206**, 299 (1989).

[29] F. Reuter and R. Mettin, Mechanisms of single bubble cleaning, Ultrason. Sonochem. **29**, 550 (2016).

[30] M. Koch, C. Lechner, F. Reuter, K. Köhler, R. Mettin, and W. Lauterborn, Numerical modeling of laser generated cavitation bubbles with the finite volume and volume of fluid method, using OpenFOAM, Comput. Fluids. **126**, 71 (2016).

[31] P. Marmottant and S. Hilgenfeldt, Controlled vesicle deformation and lysis by single oscillating bubbles, Nature **423**, 153 (2003).

[32] P. Tho, R. Manasseh, and A. Ooi, Cavitation microstreaming patterns in single and multiple bubble systems, J. Acoust. Soc. Am. **122**, 3051 (2007).

[33] J. Collis, R. Manasseh, P. Liovic, P. Tho, A. Ooi, K. Petkovic-Duran *et al.*, Cavitation microstreaming and stress fields created by microbubbles, Ultrasonics **50**, 273 (2010).

[34] M. S. Longuet-Higgins, Viscous streaming from an oscillating spherical bubble, Proc. R. Soc. A Math. Phys. Eng. Sci. **454**, 725 (1998).

[35] M. S. Plesset and A. Prosperetti, Bubble dynamics and cavitation, Annu. Rev. Fluid Mech. **9**, 145 (1977).

[36] H. Lin, B. D. Storey, and A. J. Szeri, Rayleigh-Taylor instability of violently collapsing bubbles, Phys. Fluids. **14**, 2925 (2002).

[37] A. Philipp and W. Lauterborn, Cavitation erosion by single laser-produced bubbles, J. Fluid Mech. **361**, 75 (1998).

[38] R. Dijkink and C.-D. Ohl, Measurement of cavitation induced wall shear stress, Appl. Phys. Lett. **93**, 254107 (2008).

[39] C.-D. Ohl, M. Arora, R. Ikink, N. de Jong, M. Versluis, M. Delius *et al.*, Sonoporation from jetting cavitation bubbles, Biophys. J. **91**, 4285 (2006).

[40] K. R. Rau, P. A. Quinto-Su, A. N. Hellman, and V. Venugopalan, Pulsed laser microbeam-induced cell lysis: Time-resolved imaging and analysis of hydrodynamic effects, Biophys. J. **91**, 317 (2006).

[41] Y. Arita, M. Antkowiak, V. Venugopalan, F. J. Gunn-Moore, and K. Dholakia, Dynamics of primary and secondary microbubbles created by laser-induced breakdown of an optically trapped nanoparticle, Phys. Rev. E **85**, 016319 (2012).

[42] F. Reuter, C. Cairós, and R. Mettin, Vortex dynamics of collapsing bubbles: Impact on the boundary layer measured by chronoamperometry, Ultrason. Sonochem. **33**, 170 (2016).

[43] G. L. Chahine, A. Kapahi, J.-K. Choi, and C.-T. Hsiao, Modeling of surface cleaning by cavitation bubble dynamics and collapse, Ultrason. Sonochem. **29**, 528 (2016).

[44] A. Vogel and W. Lauterborn, Time-resolved particle image velocimetry used in the investigation of cavitation bubble dynamics, Appl. Opt. **27**, 1869 (1988).

[45] D. Kröninger, K. Köhler, T. Kurz, and W. Lauterborn, Particle tracking velocimetry of the flow field around a collapsing cavitation bubble, Exp. Fluids. **48**, 395 (2010).

[46] M. S. Longuet-Higgins, Bubbles, breaking waves and hyperbolic jets at a free surface, J. Fluid Mech. **127**, 103 (1983).

[47] M. Rattray, *Perturbation Effects in Cavitation Bubble Dynamics* (California Institute of Technology, USA, 1951).

[48] See Supplemental Material at http://link.aps.org/supplemental/10.1103/PhysRevFluids.2.064202 for videos of bubble dynamics and time resolved Lagrangian ink maps.

[49] E. Zwaan, S. Le Gac, K. Tsuji, and C.-D. Ohl, Controlled Cavitation in Microfluidic Systems, Phys. Rev. Lett. **98**, 254501 (2007).

[50] M. Minnaert, On musical air-bubbles and the sounds of running water, London, Edinburgh, Dublin Philos. Mag. J. Sci. **16**, 235 (1933).

[51] P. Saffman, *Vortex Dynamics, 1. Edition* (Cambridge University Press, Cambridge, 1995).

[52] K. Shariff and A. Leonard, Vortex rings, Annu. Rev. Fluid Mech. **24**, 235 (1992).

[53] T. T. Lim and T. B. Nickels, Vortex rings, in *Fluid Vortices*, edited by S. I. Green (Springer, Netherlands, 1995), pp. 95–153.

[54] I. S. Sullivan, J. J. Niemela, R. E. Hershberger, D. Bolster, and R. J. Donnelly, Dynamics of thin vortex rings, J. Fluid Mech. **609**, 319 (2008).

[55] P. G. Saffman, The velocity of viscous vortex rings, Stud. Appl. Math. **49**, 371 (1970).

[56] T. Maxworthy, The structure and stability of vortex rings, J. Fluid Mech. **51**, 15 (1972).

[57] F. Marken, J. C. Eklund, and R. G. Compton, Voltammetry in the presence of ultrasound: Can ultrasound modify heterogeneous electron transfer kinetics? J. Electroanal. Chem. **395**, 335 (1995).

[58] T. J. Mason and J. P. Lorimer, *Applied Sonochemistry* (Wiley-VCH Verlag GmbH & Co. KGaA, Weinheim, FRG, 2002).

[59] H. Feng, G. Barbosa-Canovas, and J. Weiss (eds.), *Ultrasound Technologies for Food and Bioprocessing* (Springer, New York, 2011).

[60] F. Touyeras, J. Y. Hihn, X. Bourgoin, B. Jacques, L. Hallez, and V. Branger, Effects of ultrasonic irradiation on the properties of coatings obtained by electroless plating and electro plating, Ultrason. Sonochem. **12**, 13 (2005).

[61] A. J. Cobley, T. J. Mason, and V. Saez, Review of effect of ultrasound on electroless plating process, Trans. Inst. Met. Finish. **89**, 303 (2011).

[62] H. Monnier, A. M. Wilhelm, and H. Delmas, Influence of ultrasound on mixing on the molecular scale for water and viscous liquids, Ultrason. Sonochem. **6**, 67 (1999).

[63] J. Lee, M. Ashokkumar, and S. E. Kentish, Influence of mixing and ultrasound frequency on antisolvent crystallisation of sodium chloride, Ultrason. Sonochem. **21**, 60 (2014).

[64] J. Jordens, B. Bamps, B. Gielen, L. Braeken, and T. Van Gerven, The effects of ultrasound on micromixing, Ultrason. Sonochem. **32**, 68 (2016).

[65] J. M. Commenge and L. Falk, Villermaux-Dushman protocol for experimental characterization of micromixers, Chem. Eng. Process. Process Intensif. **50**, 979 (2011).

[66] J. Aubin, M. Ferrando, and V. Jiricny, Current methods for characterising mixing and flow in microchannels, Chem. Eng. Sci. **65**, 2065 (2010).

[67] E. Pairam and A. Fernández-Nieves, Generation and Stability of Toroidal Droplets in a Viscous Liquid, Phys. Rev. Lett. **102**, 234501 (2009).

[68] B. Darbois Texier, K. Piroird, D. Quéré, and C. Clanet, Inertial collapse of liquid rings, J. Fluid Mech. **717**, R3 (2013).

[69] D. T. H. New and S. C. M. Yu, *Vortex Rings and Jets* (Springer Singapore, Singapore, 2015).

[70] S. H. Yang, S. Y. Jaw, and K. C. Yeh, Single cavitation bubble generation and observation of the bubble collapse flow induced by a pressure wave, Exp. Fluids. **47**, 343 (2009).

[71] Q. X. Wang, K. S. Yeo, B. C. Khoo, and K. Y. Lam, Nonlinear interaction between gas bubble and free surface, Comput. Fluids. **25**, 607 (1996).

[72] M. Lee, E. Klaseboer, and B. C. Khoo, On the boundary integral method for the rebounding bubble, J. Fluid Mech. **570**, 407 (2007).

[73] Q. X. Wang, Non-spherical bubble dynamics of underwater explosions in a compressible fluid, Phys. Fluids. **25**, 072104 (2013).

[74] A. M. Zhang, S. Li, and J. Cui, Study on splitting of a toroidal bubble near a rigid boundary, Phys. Fluids **27**, 62102 (2015).

[75] M. Holt, Underwater explosions, Annu. Rev. Fluid Mech. **9**, 187 (1977).

[76] P. E. Dimotakis, Turbulent mixing, Annu. Rev. Fluid Mech. **37**, 329 (2005).

[77] C. D. Ohl and R. Ikink, Shock-Wave-Induced Jetting of Micron-Size Bubbles, Phys. Rev. Lett. **90**, 214502 (2003).

[78] D. Obreschkow, M. Tinguely, N. Dorsaz, P. Kobel, A. de Bosset, and M. Farhat, Universal Scaling Law for Jets of Collapsing Bubbles, Phys. Rev. Lett. **107**, 204501 (2011).

[79] S. T. Wereley and C. D. Meinhart, Micron-resolution particle image velocimetry, in *Microscale Diagnostic Techniques* (Springer-Verlag, Berlin/Heidelberg, 2005), pp. 51–112.